

# Towards monitoring CO<sub>2</sub> source-sink distribution over India via inverse modelling: Quantifying the fine-scale spatiotemporal variability of atmospheric CO<sub>2</sub> mole fraction

5 Vishnu Thilakan<sup>1,4</sup>, Dhanyalekshmi Pillai<sup>1,4</sup>, Christoph Gerbig<sup>2</sup>, Michal Galkowski<sup>2,3</sup>,  
Aparna Ravi<sup>1,4</sup>, and Thara Anna Mathew<sup>1</sup>

<sup>1</sup>Indian Institute of Science Education and Research Bhopal (IISERB), Bhopal, India

<sup>2</sup>Max Planck Institute for Biogeochemistry, Jena, Germany

<sup>3</sup>AGH University of Science and Technology, Kraków, Poland

10 <sup>4</sup>Max Planck Partner Group (IISERB), Max Planck Society, Munich, Germany

*Correspondence to:* Dhanyalekshmi Pillai ([dhanya@iiserb.ac.in](mailto:dhanya@iiserb.ac.in), [kdhanya@bgc-jena.mpg.de](mailto:kdhanya@bgc-jena.mpg.de))

## Abstract

Improving the estimates of CO<sub>2</sub> sources and sinks over India through inverse methods calls for a comprehensive  
15 atmospheric monitoring system involving atmospheric transport models that make a realistic accounting of  
atmospheric CO<sub>2</sub> variability along with a good coverage of ground-based monitoring stations. This study  
investigates the importance of representing fine-scale variability of atmospheric CO<sub>2</sub> in models for the optimal  
use of observations through inverse modelling. The unresolved variability of atmospheric CO<sub>2</sub> in coarse models  
is quantified by using WRF-Chem simulations at a spatial resolution of 10 km × 10 km. We show that the  
20 representation errors due to unresolved variability in the coarse model with a horizontal resolution of one degree  
(~ 100 km) are considerable (median values of 1.5 ppm and 0.4 ppm for the surface and column CO<sub>2</sub>,  
respectively) compared to the measurement errors. The monthly averaged surface representation error reaches  
up to ~5 ppm, which is even comparable to half of the magnitude of seasonal variability or concentration  
enhancement due to hotspot emissions. Representation error shows a strong dependence on multiple factors such  
25 as time of the day, season, terrain heterogeneity, and changes in meteorology and surface fluxes. By employing  
a first-order inverse modelling scheme using pseudo observations from nine tall tower sites over India, we show  
that the Net Ecosystem Exchange (NEE) flux uncertainty solely due to unresolved variability is in the range of  
3.1 to 10.3% of the total NEE of the region. By estimating the representation error and its impact on flux  
estimations during different seasons, we emphasise the need for taking account of fine-scale CO<sub>2</sub> variability in  
30 models over the Indian subcontinent to better understand processes regulating CO<sub>2</sub> sources and sinks. The  
efficacy of a simple parameterization scheme is further demonstrated to capture these unresolved variations in  
coarse models.

## 1 Introduction

Accurate assessment of sources and sinks of CO<sub>2</sub> is essential in planning and implementing mitigation strategies  
35 for greenhouse gas emissions and associated climate change. However, estimations of CO<sub>2</sub> fluxes contain  
significant uncertainties, which increase even more with finer spatial scales such as those required for the  
climate change mitigation policies at regional and national levels (e.g., Ciais et al., 2014; Li et al., 2016;  
Cervarich et al., 2016). By using atmospheric CO<sub>2</sub> concentration measurements, the CO<sub>2</sub> fluxes can be estimated

40 by a multi-constrained observation-modelling approach, often referred to as top-down approach or inverse  
modelling (Enting, 2002). For about two decades, these top-down approaches have been widely used to  
understand the modifications in the carbon cycle through natural and anthropogenic induced environmental  
changes (Bousquet, 2000; Schimel et al., 2001; Rödenbeck et al., 2003; Patra et al., 2005). In addition to the  
observations, the inverse modelling system makes use of an atmospheric transport model (forward model),  
45 which determines the distribution of CO<sub>2</sub> concentration. Thereby, the inverse optimization approach derives the  
surface fluxes that are consistent with measured concentration. The United Nations Framework Convention on  
Climate Change (UNFCCC) has acknowledged the increasing capability of inverse modelling to systematically  
monitor greenhouse gas (GHG) concentrations (Bergamaschi et al., 2018).

Most of the inverse modelling systems rely on global atmospheric transport models with coarse horizontal  
resolution (often greater than one degree) (Rödenbeck et al., 2003; Peters et al., 2007; Rödenbeck et al., 2018a,  
50 b; Inness et al., 2019). These global data assimilation systems play an important role in studying continental or  
sub-continental fluxes at annual or sub-annual scales. However, regional estimation of fluxes using global  
models is hindered by the inability of these transport models to represent the observed CO<sub>2</sub> variability. The  
observed variability, as seen from the spatial and temporal distribution of atmospheric CO<sub>2</sub>, is highly correlated  
with the space and time scales of weather systems (Parazoo et al., 2011). This explains the presence of large  
55 model-data mismatches in regions where mesoscale circulation is predominant (Ahmadov et al., 2007). Wind  
speed, wind direction, and height of the planetary boundary layer (PBL) are the critical variables that determine  
the atmospheric CO<sub>2</sub> variability. Strong wind normalizes other small-scale variations in observed concentration  
due to mixing. In such cases, the CO<sub>2</sub> variability is expected to be dominated by the variations in background  
concentration, hence the predictability can be higher during these conditions (Sarrat et al., 2007). The height of  
60 the PBL is an essential variable since the atmospheric CO<sub>2</sub> is subjected to rapid mixing up to this altitude.  
Hence, for a given location with a negative gradient in CO<sub>2</sub> vertical distribution, an overestimation of PBL  
height leads to an underestimation of CO<sub>2</sub> concentration and vice-versa (Gerbig et al., 2008).

Another important variable that impacts the CO<sub>2</sub> variability is the heterogeneous topography. Variations in  
topography influence the transport of the tracers. When the small-scale orographic details are not adequately  
65 represented in the models, they can lead to representation errors in CO<sub>2</sub> simulations as large as 3 ppm at scales  
of 100 km (Tolk et al., 2008; Pillai et al., 2010). Horizontal gradients in CO<sub>2</sub> concentrations can go up to values  
of 30 ppm within a spatial scale of 200 km, depending on the land surface heterogeneity (van der Molen and  
Dolman, 2007). Furthermore, variations in land use patterns between neighbouring regions can cause  
considerable variability in the CO<sub>2</sub> surface fluxes. Thus, a proper representation of land use patterns is also  
70 important in terms of simulating CO<sub>2</sub> variability. Previous studies based on airborne measurements reported that  
transport models need a spatial resolution smaller than 30 km to be able to represent CO<sub>2</sub> spatial variability in  
the continental boundary layer (Gerbig et al., 2003). Significant efforts have been invested in deriving fluxes by  
taking into account these fine-scale variations (e.g., Gerbig et al., 2003; Lauvaux et al., 2009a; Carouge et al.,  
2010; Pillai et al., 2011, 2012; Broquet et al., 2013) over North American and Eurasian domains in the past  
75 decade. However, there still exists lower confidence in estimates over other regions, where there is a lack of  
both advanced modelling systems at relevant spatio-temporal resolutions and good coverage of ground-based  
monitoring stations.

In the context of the Indian sub-continent, the inverse-based estimation of fluxes at fine scales is essentially new; hence many questions remain. A number of monitoring sites measuring atmospheric greenhouse gases  
80 have become available in India during the last decade (Tiwari et al., 2011; Lin et al., 2015, Nomura et al., 2021). Aside from the ongoing progress in augmenting observational data streams, it remains challenging to assimilate these data for deducing process-specific information effectively (e.g., McKain et al., 2012; Bréon et al., 2015; Pillai et al., 2016). The limitation of coarse global models in representing observations over the Indian subcontinent is reflected in the analysis made by Patra et al. (2011).

85 The seasonally reversing South Asian monsoon system is a prominent meteorological phenomenon affecting the Indian subcontinent, which is also expected to influence the terrestrial-atmosphere flux exchanges. Various studies have demonstrated the role of Indian monsoon circulations on regional atmospheric transport by strong south westerly winds during the summer monsoon (June to September) and by north easterly winds during the winter monsoon (October to November) (e.g., Goswami and Xavier, 2005; Krishnamurthy and Shukla, 2007).  
90 Monsoon convection transports the boundary layer air into the upper troposphere. Subsequently, air parcels are slowly uplifted by diabatic heating to higher altitudes (e.g., Vogel et al., 2019). An accurate representation of convective vertical transport is very challenging and an important source of uncertainty in current transport models (Willettts et al., 2016). Note that the Asian summer monsoon anticyclone (ASMA) active during the Indian summer monsoon period plays a key role in uplifting trace gases to the upper troposphere and lower  
95 stratosphere (e.g., Park et al., 2007). Moreover, a significant component of flux variations can arise from biospheric fluxes (Schimel et al., 2014), which is influenced by variables such as rainfall, radiation, and temperature (Chen et al., 2019). Several studies showed that the monsoon system substantially impacts vegetation growth, generating distinct spatio-temporal patterns of the biogenic fluxes (e.g., Gadgil, 2003; Valsala and Maksyutov, 2013, Ravi Kumar et al., 2016, Kunchala et al., 2022). It is noteworthy that the cropping patterns over India have a strong dependence on seasons and are mainly determined by dry and wet  
100 seasons for nearly 65 to 70 % of the country's area except over north-eastern and south-western (Western Ghats) regions of India. In India, wet season crops (Kharif crops cultivated from June to November) including Rice, Millets, and Maize mainly depend on monsoon rain. Dry season crops (Rabi crops, e.g. Wheat, Barley, and Mustard, cultivated from November to April,) are less water-dependent and primarily rely on irrigation  
105 (DAC/MA 2015). Therefore, employing a higher resolution modelling over the Indian subcontinent is desirable to better account for fine-scale variations generated by both mesoscale transport processes and surface flux patterns.

This study focuses on accounting for unresolved sub-grid scale variability when employing current generation  
110 global models. Assimilation of observations in an inverse framework requires the characterization of these error structures at relevant scales that can be utilized to retrieve source-sink distribution over India. The main objectives of this paper are to describe and quantify the expected spatiotemporal variability of atmospheric CO<sub>2</sub> that is not resolved by the current generation global models, quantify to what extent these variations cause uncertainty in flux estimations, and assess how these uncertainties can be minimized by modelling the sub-grid variations in the global models. Specifically, we address the following questions: 1) how good is the level of  
115 agreement among global transport models that are used in current generation inversion systems for predicting atmospheric CO<sub>2</sub> concentrations over the Indian subcontinent? 2) how large are the variations of atmospheric

CO<sub>2</sub> that are unresolved by global and regional models, which operate at different spatial scales from 4°× 4° to 0.5°× 0.5° ? 3) what is the role of seasonal changes on generating different patterns in these sub-grid variations of CO<sub>2</sub>? 4) how much is the uncertainty in the inverse-based flux estimation caused by these unresolved variations in the coarse models when utilizing a given network of surface observations over the domain? 5) how effectively can we capture the key aspects of the variability and account for it in flux estimations? Information from observations can be better utilized if we improve the atmospheric transport models to resolve the observed variability as accurately as possible. As a result, the data assimilation system gains significantly (e.g. with increasing weights on observations and performing minimal data filtering), from this for improving the flux estimates.

In this article, we present results based on the analyses of high-resolution simulations at a spatial resolution of 10 km × 10 km for the months of July and November 2017. The year 2017 was characterized by neutral Indian Ocean Dipole conditions over the Indian Ocean with the beginning of a mild La Nina over the Pacific by the end of the year (NOAA/ESRL, 2022a, b). The month of July represents a monsoon period when both biospheric and convective activity are strong. July is also characterized by strong low-pressure system activity over the Bay of Bengal, which results in large rainfall over central India (Krishnamurthy and Ajayamohan, 2010). In contrast, the month of November is more representative of post-monsoon wintertime over the Indian subcontinent. We quantify the expected sub-grid variability using our high-resolution simulations. We have also utilized optimized CO<sub>2</sub> products at global scales to provide a more comprehensive overview of the typical mismatch among the existing model simulations over the Indian subcontinent even at monthly and annual scales. A part of these mismatches can be arisen due to the inability of coarse resolution global models to simulate the sub-grid scale processes which can lead to representation errors; thus, uncertainty in inverse estimations. By designing a pseudo surface observation network over the domain, we investigate the impact of these unresolved variations on the regional flux estimations and assess how a simple parameterization scheme can help in reducing these errors in the global model. To our knowledge, there is no comprehensive published study of this kind over the Indian subcontinent until now assessing the magnitude and impact of temporal and spatial variability exhibited by atmospheric CO<sub>2</sub>.

The outline of the paper (see Supplementary Fig. S1) is as follows: Section 2 describes our modelling system, data and methods used for reporting inter-model mismatches and quantifying the sub-grid scale variability CO<sub>2</sub>. In Sect. 3, we present our analysis, demonstrating the impact of unresolved sub-grid scale variability on CO<sub>2</sub> flux estimation over India. Finally, we discuss the implications of our findings in Sect. 4, highlighting possible ways forward to yield an improved estimation of CO<sub>2</sub> budgets over India.

## 2 Data & Methodology

In the following subsections, we describe our high-resolution modelling system (Sect. 2.1), existing optimized global CO<sub>2</sub> simulations used in the study (Sect. 2.2), quantification of representation error (Sect. 2.3), and the observation system simulation experiment (OSSE) designed to estimate the impact of the derived sub-grid scale variations on flux estimations over India via inverse optimization (Sect. 2.4).

## 2.1 WRF-Chem GHG Modelling System

155 We use the modelling system WRF-Chem GHG in which the Weather Research and Forecasting model (WRF) version 3.9.1.1 (Skamarock et al., 2008) is coupled with the greenhouse gas module (WRF-Chem-GHG, Beck et al., 2011), implemented as part of the WRF-Chem distribution (WRF-Chem, Grell et al., 2005). For simulating the atmospheric transport, the model uses fully compressible Eulerian non-hydrostatic equations on Arakawa C-staggered grid, conserving mass, momentum and scalars (Skamarock et al., 2008). In the WRF-Chem GHG  
160 (hereafter referred as WRF-GHG), we use the passive tracer chemistry option to simulate changes in CO<sub>2</sub> mixing ratios associated with surface fluxes and atmospheric transport. We utilize a biospheric model and emission inventory data to simulate atmospheric CO<sub>2</sub> enhancements associated with biogenic and emission fluxes as described in Sect. 2.1.1 and 2.1.2. Table. 1 summarizes the model configuration, including physics parameterizations and input data used in this study.

165 The model domain covers a region spanning from 65°E to 100°E and 5°N to 40°N, configured in a Lambert conformal conic (LCC) projection with 307 × 407 grid points. The spatial resolution of the grid is 10 km × 10 km, and the model time-step is 60 s. We have used model output with a temporal resolution of 1 hour for this study. The simulations are performed using 39 vertical levels with the model top at 50 hPa and 10 levels within the lowest 2 km. WRF-GHG simulations are performed for the entire July and November 2017. Implementation  
170 of the WRF-GHG system over the Indian subcontinent enables us to customize it according to the domain features and build a state-of-the-art modelling system, which eventually estimates CO<sub>2</sub> fluxes through regional inverse systems. The potential of the WRF-GHG model in simulating fine-scale spatial variability was also established in previous studies (Ahmadov et al., 2009; Pillai et al., 2011; Park et al., 2018).

### 2.1.1 Representation of biospheric fluxes

175 We use the Vegetation Photosynthesis and Respiration Model (VPRM) in the modelling system to calculate Net Ecosystem Exchange (NEE) representing the biospheric fluxes (Mahadevan et al., 2008). VPRM is a diagnostic biosphere model, which utilizes remote sensing products: Enhanced Vegetation Index (EVI) and Land Surface Water Index (LSWI) derived from reflectance data of the Moderate resolution Imaging Spectroradiometer (MODIS) as well as meteorological data: solar radiation and air temperature. In this study, these hourly NEE  
180 calculations are performed within WRF-GHG, simultaneously with the meteorology simulations in which NEE is calculated as a sum of gross ecosystem exchange (GEE) and ecosystem respiration ( $R_{eco}$ ). VPRM, in this case, uses the meteorological data provided by WRF-GHG. VPRM uses the SYNMAP vegetation classification (using the tile approach) (Jung et al., 2006) as well as EVI and LSWI from MODIS surface reflectance data at a resolution of 1 km and 8 days. We aggregate these indices specific for different vegetation types onto the LCC  
185 projection for the entire domain at the model's spatial resolution. A number of studies have used VPRM for other regions around the world in which derived NEE shows good prediction skills for hourly to monthly timescales (Ahmadov et al., 2009; Pillai et al., 2011; Liu et al., 2018; Park et al., 2018).

### 2.1.2 Representation of emission fluxes

Anthropogenic CO<sub>2</sub> emission fluxes are prescribed from the Emission Database for Global Atmospheric  
190 Research (EDGAR) dataset, version 6.0, provided at a horizontal resolution of 0.1° × 0.1° (Crippa et al., 2021).

We disaggregate the available annual emission data into hourly emissions using the temporal distribution CO<sub>2</sub> profiles (Steinbach et al., 2011; Kretschmer et al., 2014). To represent biomass burning emission, we have used data from the Global Fire Assimilation System (GFAS) with a spatial resolution of 0.1° × 0.1° and a temporal resolution of one day. GFAS is based on satellite data, which provides the fire emission by assimilating fire radiative power (FRP) observations from MODIS instruments (Kaiser et al., 2012). All these flux data are gridded and projected to WRF-GHG's model domain.

### 2.1.3 Initial and boundary conditions

Meteorological and chemical initial and boundary conditions are required in WRF-GHG to account for the initial state and inflow or background flow. The initial and lateral boundary conditions for the meteorological variables, including horizontal wind components, pressure, specific humidity, sea surface temperature (SST), and the necessary surface initialization fields are obtained from the ERA5 reanalysis dataset of the European Centre for Medium-Range Weather Forecasts (ECMWF), extracted at a horizontal resolution of 25 km and a temporal resolution of 1 hour (Hersbach et al., 2020). The initial and lateral boundary conditions of CO<sub>2</sub> tracers are obtained from the Copernicus Atmosphere Monitoring Service (CAMS) global greenhouse gas forecast products (currently in development, see Massart et al., 2016; Agusti-Panareda et al., 2019). Namely, we have used the dry air mole fractions of CO<sub>2</sub> from the CAMS greenhouse gas experiment analysis (gqiq), with a temporal resolution of 6-hour, horizontal resolution of 0.5° × 0.5° (original resolution 9 km × 9 km) and 137 vertical levels. Note that the CAMS product at 9 km × 9 km resolution is in the developmental phase and not yet available to the general public (personal contact: Anna.Agusti-Panareda@ecmwf.int).

We have utilized a simulation strategy to update the initial meteorological conditions for taking advantage of assimilated meteorological fields from ECMWF. The model is reinitialized each day with ECMWF assimilated data at the model starting time of 12.00 UTC (day+0) and runs for 30 hours until 18:00 UTC of the next day (day+1). The first six hours are considered for meteorological spin-up, and the remaining 24 hours (from day+0,18:00 UTC to day+1, 18:00 UTC) are used for the analysis. The initialization of CO<sub>2</sub> is done at the beginning of the first hour of model simulation, which is 00:00 UTC (e.g., Ahmadov et al., 2012; Pillai et al., 2011).

### 2.2 Global model products

We have used optimized products at global scales to examine the differences in the representation of CO<sub>2</sub> variability over the Indian subcontinent at monthly and annual scales. These global model outputs are derived from inverse model simulations, which estimate the source-sink distributions of CO<sub>2</sub> and then generate three-dimensional CO<sub>2</sub> concentration fields that are consistent with the optimized posterior fluxes. Four global inverse modelling products - CarbonTracker, CarboScope, LSCE v18r3 and LSCE FT18r1- available for the year 2017 are used for our analysis (See Table. 2 for more details). The LSCE model version v18r3 (hereafter LSCE) utilizes surface observations, and the model version FT18r1 (hereafter LSCE FT) uses satellite retrievals from the Orbiting Carbon Observatory (OCO-2) for the optimization of CO<sub>2</sub> fluxes (Chevallier et al., 2005; Chevallier et al., 2010; Chevallier, 2013). All these above models differ in terms of the model formulations and configuration (e.g., transport and the employed inversion methodology), observational datasets that were assimilated (e.g., data from surface monitoring stations, aircraft missions, ship cruises, AirCore balloon

230 soundings, and satellite’s total column retrievals), prior datasets, and spatiotemporal resolutions. None of these products used ground-based observations from the Indian subcontinent for their optimization, which raises concerns about the reliability of the optimized flux estimations over the region. Hence, it can be assumed that a part of the inter-model differences in predicting the variability is related to the paucity of CO<sub>2</sub> observations over the region. To represent the daytime, we have used the concentration fields for the local time ranging from 11:30 to 16:30 from all these models for the analysis.

### 235 2.3 Quantification of spatial variability

For quantifying the spatial variability due to sub-grid scale processes that cannot be resolved by the coarse resolution models, we follow the approach as described in Pillai et al. (2010). The term ‘representation error’ indicates the mismatch between the scales of model simulations and observations collected (Pillai et al., 2010; Janjić et al., 2017). In other words, the representation errors arise due to unresolved scales not captured by the  
 240 model. Here we calculate the representation errors in the coarse resolution models, which can be resolved by implementing a high-resolution model at 10 km resolution. It is assumed that the high-resolution simulation captures the majority of the sub-grid scale variability even though it cannot be expected to resolve all observed variability. Most of the current global model simulations are performed at coarse resolutions of several degrees. But with the recent advancement in computational capacity and numerical techniques, a horizontal resolution of  
 245 1° × 1° is quite likely achievable for the global data assimilation systems. For estimating the representation error in a coarse model with a typical spatial resolution of 1° × 1°, we have calculated the standard deviation of CO<sub>2</sub> dry air mole fraction simulated by the WRF-GHG model within the coarse grid boxes of 1° × 1° as follows:

$$\sigma_{CO_2(\text{tot})} = \sqrt{\frac{1}{n-1} \sum_{j=1}^n (m_j - \bar{m})^2} \quad (1)$$

250 where  $\bar{m} = \frac{1}{n} \sum_{j=1}^n m_j$

$n$  is the number of 10 km boxes inside the coarser grid cell of 1° × 1°;  $m$  is the CO<sub>2</sub> dry air mole fraction corresponding to 10 km boxes; and  $\bar{m}$  is the average within the coarser grid cell. So, the estimated values represent the sub-grid scale variability within the coarse model grid cell with a horizontal resolution of 1° × 1°. The representation errors are calculated at corresponding vertical model levels to represent the impact of surface  
 255 influence and mesoscale transport adequately as predicted by the high-resolution model. As mentioned before, we assume that the high-resolution simulations represent the realistic distribution of CO<sub>2</sub>. Further, we assume that the coarse resolution model also has a terrain-following vertical coordinate system and also has the same vertical grid spacing of high-resolution model. As space-borne instruments measure total columns rather than near-surface concentrations, we extend the analysis to column-averaged dry air mole fraction (XCO<sub>2</sub>) as  
 260 measured by the satellite instrument. i.e.,  $m$  represents either CO<sub>2</sub> at a given model level or XCO<sub>2</sub>. In order to assess the dependence of representation errors on the horizontal resolution of the employed model, we have computed representation errors for multiple resolutions ranging from 0.5° × 0.5° to 4° × 4°, in addition to 1° × 1°, which would encompass the resolutions of both present and near-future global inverse modelling systems.

265 The surface representation errors are calculated using the model simulations from the second model level (mean height is ~200 m from sea level) to avoid the inconsistency that can be generated from inputting emission fluxes at the first model level. Representation errors are calculated separately for daytime (11:30 to 16:30 local time) and nighttime (23:30 to 4:30 local time) to account for the difference in sub-grid scale process during these times. The representation error presented in Eq. (1) varies from one model time step to the next. In order to  
 270 obtain a typical (average) representation error, we compute the monthly average representation error ( $\sigma_{CO_2}$ ) using Eq. (2).

$$\sigma_{CO_2} = \frac{1}{T} \sum_{t=1}^T \sigma_{CO_2(tot)} \quad (2)$$

where T is the total number of simulations in a month during daytime or nighttime. Further, we have calculated the representation error ( $\sigma_{\overline{CO_2}(mon)}$ ) using Eq. (3), which describes the systematic component of representation  
 275 error and provides important constraints for inversions using both ground-based and satellite observations over India.

$$\sigma_{\overline{CO_2}(mon)} = \sqrt{\frac{1}{n-1} \sum_{j=1}^n (M_j - \overline{M})^2} \quad (3)$$

$$\text{where } \overline{M} = \frac{1}{n} \sum_{j=1}^n M_j$$

$n$  is the number of 10 km boxes inside the coarser grid cell of  $1^\circ \times 1^\circ$ ;  $M_j$  is the monthly averaged  $CO_2$  dry air  
 280 mole fraction at a 10 km spatial scale; and  $\overline{M}$  is the corresponding average within the coarser grid cell of  $1^\circ$ . The difference between Eq. (1) and Eq. (3) is that we use monthly averaged  $CO_2$  concentration values in Eq. (3) instead of hourly values as in Eq. (1). Both July and November are used to understand the differences in the variability during summer and winter.

Due to the paucity of adequate ground-level observations over India, satellite observations play an essential role  
 285 in the estimation of  $CO_2$  fluxes via inverse modelling (e.g. Philip et al., 2022). Satellite observations can provide column average  $CO_2$  ( $XCO_2$ ) concentration with a precision of 1 to 1.5 ppm (O'Dell et al., 2012; Wunch et al., 2017; Liang et al., 2017). In order to utilize these satellite observations, the transport models being used in the inverse estimation must be highly accurate. Since satellite footprints are smaller ( $\sim 2 - 20 \text{ km}^2$ ) than the current model grid size ( $> 100 \text{ km}$ ), using these measurements for optimization via inverse modelling introduces spatial  
 290 representation errors and associated uncertainties in the inferred fluxes. Note that the spatial biases of a few tenths of a ppm in column-averaged  $CO_2$  can potentially alter even the annual sub-continental fluxes in the range of tenths of a gigaton of carbon fluxes (Chevallier et al., 2007, Miller et al., 2007 and Chevallier et al., 2010). To quantify these systematic transport errors when representing satellite measurements in inverse models, we calculate the spatial representation errors for  $XCO_2$  that coarse inverse modelling would suffer from  
 295 using highly precise and accurate satellite measurements.

We have selected monsoon (July) and post-monsoon (November) periods for our analysis to identify the seasonal differences in the sub-grid variability over India. In July, many low-pressure systems were active in the

monsoon trough region (IMD weather reports, <https://mausam.imd.gov.in>). In general, tropical cyclones in the Asian monsoon region can cause fast uplift of air masses into the upper troposphere and lower stratosphere (e.g. Li et al., 2021), which may increase the modelling error due to the misrepresentation of the associated convective activity that is only parameterized in global models. The presence of enhanced biospheric activity during July can reduce the CO<sub>2</sub> concentration in the lower troposphere (e.g. Patra et al., 2011). Also, the strong vertical and horizontal mixing due to the monsoon circulation dilutes the CO<sub>2</sub> concentration in the atmosphere during July compared to November. The convective activity associated with the Indian summer monsoon was absent during November, however the convection caused by synoptic systems such as tropical cyclones was still present. Such a low-pressure system activity was found over the Bay of Bengal and over the Lakshadweep area ( $\approx 8^\circ$  N,  $74^\circ$  E) from 22<sup>nd</sup> November onwards. One of these low-pressure systems in the Bay of Bengal further developed and intensified as a deep depression and moved to the southeast Arabian Sea and evolved into a severe cyclonic storm (Ockhi) by 30<sup>th</sup> November.

#### 310 **2.4 Estimation of representation error induced flux uncertainty using pseudo surface measurements**

In order to quantify the impact of representation errors on flux estimations when utilizing surface measurements, we have devised the following strategy. We used nine CO<sub>2</sub> surface monitoring sites representing various geographical regions in India (Fig. 1). Not all these observation stations are currently fully operational or have continuous measurements. We have performed an observation system simulation experiment (OSSE) using high-resolution CO<sub>2</sub> simulations generated by the WRF-GHG model for each of these stations. We focus on the biospheric flux component, NEE. The simulated values of coarse models to compare with the observations are obtained from the nine grid cells of the coarse model covering these sites. The pseudo observations for these sites correspond to the values simulated by the WRF-GHG model at one of the fine grid cells contained in one cell of the coarse model. Since there are 100 fine grid cells per coarse grid cell, 100 different time series are generated and 100 corresponding inversions are performed to obtain robust results. For deducing the contribution of the representation error to the biospheric flux uncertainty, we have taken the following assumptions: 1) the hourly WRF-GHG simulations at 10 km ( $\sim 0.1^\circ$ ) spatial scale represents actual variations in CO<sub>2</sub> mixing ratios of the measurement site, 2) there are no model or observation errors other than representation error, 3) the model captures the spatial and temporal patterns of fluxes correctly, and 4) the contribution from other surface fluxes and background mixing ratio (in ppm) are known. As a first-order simplification for the inversion, we assume that the footprints of each observation site span a radius of 200 km around the site based on our analysis using the Stochastic Time-Inverted Lagrangian Model (STILT, Lin et al., 2003). STILT footprints indicate that 50% of the sensitivity of a site to fluxes over India is located in a region that has about the same area as a circle with a radius of 200 km. For nine stations, this footprint area covers around 35 % of the total area of India. The STILT is driven with ECMWF IFS (Integrated Forecasting System) meteorological fields and the trajectories are calculated based on 100 virtual particles that are released for each time interval and location. The residence time of particles in the surface layer is weighted by the atmospheric density to derive the footprints of each location.

In our inversion set-up, we have used the hourly biospheric contribution of the atmospheric CO<sub>2</sub> mixing ratios simulated by WRF-GHG over the coarse grid cell of  $1^\circ \times 1^\circ$  surrounding the location of each measurement site as OSSE observations ( $m_{i,j}(t)$ ).

$$y_{i,j}(t) \equiv m_{i,j}(t) = \mathbf{H}_{i,j}(t) \cdot \mathbf{F}(\boldsymbol{\lambda}) \quad (4)$$

where  $\mathbf{H}$  is the transport operator and  $\mathbf{F}(\boldsymbol{\lambda})$  is the flux model in which a subset of parameters  $\boldsymbol{\lambda}$  out of total model parameters  $\mathbf{p}$  will be optimized in the inversion. Here,  $i$  ( $i=1$  to 9) represents the nine observation sites and  $j$  ( $j=1$  to 100) is the number of WRF-GHG pixels inside the coarser grid cell of  $1^\circ \times 1^\circ$ .

The modelled biospheric CO<sub>2</sub> signal ( $\bar{m}_i$ ) for the inversion is given by:

$$\bar{m}_i(t) = m_{i,j}(t) + \boldsymbol{\varepsilon}_{i,j}(t) \quad (5)$$

The modelled values deviate from the observations by a representation error  $\boldsymbol{\varepsilon}_{i,j}(t)$ . Since the modelled values ( $\bar{m}_i$ ) correspond to the mean of the 100 fine grid cells, the simulated values at site  $i$  are given as:

$$\bar{m}_i(t) = \frac{1}{100} \sum_1^{100} m_{i,j}(t) \quad (6)$$

Here,  $\mathbf{F}(\boldsymbol{\lambda})$  is taken as linearly dependent on  $\boldsymbol{\lambda}$ ; hence can be expressed as

$$\mathbf{F}(\boldsymbol{\lambda}) = \boldsymbol{\Phi} \cdot \boldsymbol{\lambda} \quad (7)$$

where  $\boldsymbol{\Phi}$  is the biospheric flux (NEE) distribution over the region.

In the inversion, we retrieve monthly NEE by utilizing hourly  $m_{i,j}(t)$  and  $\bar{m}_i(t)$  over a month. For OSSE and uncertainty flux estimation, we use the VPRM-derived NEE fluxes as the “true” fluxes (see Sect. 2.1.1). By this inverse modelling design, we require to perform 100 inversions per site, each of which uses a realization of representation error to estimate the corresponding realization of the resulting uncertainty in the retrieved fluxes.

Both the observation and simulation vector have 6480 ( $=9 \times 30 \times 24$ ) elements for a month having 30 days, and the state vector has 9 elements corresponding to scaling factors of fluxes for that month over regions around the 9 sites (see Fig. 1). In other words, each site has been assigned with one scaling factor for NEE, and there is a total of 9 scaling factors for a given month. We use a unit vector  $\boldsymbol{\lambda}$  as prior scaling factors. The prior uncertainty is neglected here, as the expected impact of the representation error on the retrieved fluxes is significantly smaller than typical prior uncertainties assumed in Bayesian inversions (on the order of 50% – 100% for biospheric fluxes). Hence neglecting this prior uncertainty does not have a large impact on our results. The inversion retrieves optimized scaling factors  $\boldsymbol{\lambda}_{retr}$ .

We have performed 100 inversions per site, and the scaling factors are retrieved by minimising the cost function for each observation station:

$$J(\lambda_{i,j}) = \frac{1}{T} \sum_{t=1}^T (m_{i,j}(t) - \bar{m}_i(t)\lambda_{i,j})^2 \quad (8)$$

where  $T$  is the number of observations for a month. Minimizing these cost functions results in an optimized estimate of scaling factors  $\boldsymbol{\lambda}_{retr}$ , which is a vector of scaling factors with nine elements ( $\lambda_{retr,i}$ ) for each of the 100 inversion cases.

By this inverse design, the deviation of posterior fluxes from the true fluxes over India is thus the uncertainty in retrieved fluxes,  $\mathbf{S}_{rep}$ , that arises solely due to the contribution from the representation error. Standard deviation  
 370 of the scaling factors from these 100 inversions ( $\sigma_{\lambda_{retr}}$ ) are used to retrieve flux uncertainty.  $\mathbf{S}_{rep}$  is obtained as follows:

$$\mathbf{S}_{rep} = \sqrt{\sum_{k=1}^K (\mathbf{S}_{\lambda_{retr},k} \Phi_{true,k})^2} \quad (9)$$

where  $\Phi_{true}$  is the monthly VPRM biospheric flux (NEE) over the Indian region and  $k$  is the number of pixels  
 (33141 pixels) over the Indian region. Here,  $\mathbf{S}_{\lambda_{retr}}$  has the dimension of Indian region at a 10 km spatial  
 375 resolution and is defined in such a way that all the grid cells (at 10 km spatial resolution) other than the grid  
 cells within the influence region (200 km radius around the station) of each station is given with zero values  
 (21335 pixels) and the grids in the influence region of each station (11806 pixels) is given with the  
 corresponding values of  $\sigma_{\lambda_{retr},i}$ . This way, the approach doesn't depend on Eq. (1) to Eq. (3), but shows the  
 impact of difference between  $m_j$  and  $\bar{m}$  on retrieved fluxes.

380 Any temporal correlations in the representation error are not considered for this experiment. We have performed  
 the inversion separately for daytime and nighttime values to identify the impact of diurnal variations of  
 representation errors on flux uncertainty. Note that by following the above inversion design and assumptions,  
 there is a high likelihood of underestimating the impact of the modelling error on flux estimations since we have  
 not considered other sources of uncertainties such as model transport uncertainty and inappropriate prior  
 385 assumptions. Thus, the quantification of flux uncertainty using this approach may be considered as the lower  
 bound of the uncertainty (i.e., the minimum flux uncertainty one may expect while estimating fluxes using a  
 model with a grid cell of  $1^\circ \times 1^\circ$  and 9 stations with the representativeness of 200 km).

### 3 Results and Discussions

#### 3.1 Agreement among global models

390 We first analyse the level of agreement among current-generation global transport models in simulating  $\text{CO}_2$   
 concentration over the Indian subcontinent. Note that a mere agreement among the coarse models does not  
 guarantee a good model performance over the region due to their plausibly large model errors in common and  
 interdependency in terms of data sources. We restrict this analysis to daytime-only values since different  
 processes control the variability of  $\text{CO}_2$  concentration at daytime and nighttime, and simulating nighttime  
 395 variability is more complicated than the daytime (Lauvaux et al., 2009a). For a consistent comparison among  
 global models, all the products are sampled at the same time for the region spanning from  $67^\circ \text{ E}$  to  $98^\circ \text{ E}$  and  
 $7^\circ \text{ N}$  to  $38^\circ \text{ N}$ . Figure 2a depicts the annual vertical profiles of  $\text{CO}_2$  concentration, showing models' discrepancy  
 in simulating the vertical gradients in concentration values including the boundary layer and the free  
 troposphere. A notable difference is observed in the simulation of the gradient within the boundary layer. The  
 400 magnitude and the height up to which this positive gradient is observed are different for these models. LSCE  
 (both versions) has the largest positive gradient among these models ( $\sim 1\text{ppm}$ ). It shows the maximum  
 concentration at around 700 m height and then a decrease in concentration. CarbonTracker also shows this  
 positive gradient in the surface layers up to a height of 900 m. But the gradient is much smaller compared to the

405 other two models. Among these four models, CarboScope does not exhibit this tendency in the lower atmosphere. Its concentration decreases linearly from the surface as the height increases.

The seasonal variability of CO<sub>2</sub> uptake through photosynthesis, release through ecosystem respiration, and vertical transport is seen when analysing the monthly averaged CO<sub>2</sub> concentration profiles over the Indian subcontinent (Figs. 2b and 3). Comparatively lower surface CO<sub>2</sub> concentrations are found during months with an active biosphere (June to October) than the rest of the period, owing to the higher ecosystem productivity  
410 over the northern hemisphere and particularly over the Indian subcontinent in response to the availability of monsoon rainfall. Also, the presence of strong southwest monsoon winds from June to September may result in bringing CO<sub>2</sub> depleted air from the southern hemisphere and thereby lowering the CO<sub>2</sub> concentration over the domain. While comparing the seasonal maximum (May) and minimum (September) of CO<sub>2</sub> concentrations measured at the Mauna Loa observatory (MLO) located in Hawaii, Fig. 2b shows a temporal shift of around one  
415 month for exhibiting seasonal maximum (April) and minimum (August) CO<sub>2</sub> concentrations. This temporal shift is attributed to the differential impacts of anthropogenic and terrestrial ecosystem activities on atmospheric concentration as well as the long-distance transfer of atmospheric carbon dioxide to remote location (Nomura et al., 2021). MLO observations are generally representative of global mean CO<sub>2</sub> due to the minimal influence of terrestrial ecosystems and anthropogenic activities at remote location. The seasonal variation of monthly  
420 averaged CO<sub>2</sub> seen over the Indian subcontinent is mostly dominated by terrestrial carbon fluxes i.e., net ecosystem exchange (NEE) as seen from the VPRM simulations (see Supplementary Fig. S2) and as e.g. in Tiwari et al., 2013.

Further, we see a CO<sub>2</sub> vertical profile with a small vertical gradient (~0.5 ppm within an altitude range of ~500 m to 4000 m) from June to October (Fig. 3). This is likely linked to the increased convective activities  
425 associated with the monsoon. The strong vertical gradient in the surface levels as simulated by the LSCE model during the monsoon period is little plausible given the strong vertical mixing expected due to the presence of strong wind and convection. The considerable inter-model variation in monthly averaged CO<sub>2</sub> concentration profiles as predicted by different global models is problematic as it indicates significant uncertainties in flux estimations over India. A part of this discrepancy can come from the coarse resolution global model's inability  
430 to represent transport processes like convection and vertical mixing, strength and distribution of anthropogenic sources and ecosystem activities that operate at fine scales. The extent of this unresolved variability in existing global models is further explored in Sect. 3.2. The spatial distribution of CO<sub>2</sub> concentration shows structural differences among these models (see Supplementary Fig. S3), which indicates a substantial knowledge gap in models for representing atmospheric CO<sub>2</sub> variability over the Indian subcontinent. As a consequence, the  
435 country's carbon budget estimations inferred via inverse modelling can be unreliable.

### 3.2 Representation errors in global transport models

The spatio-temporal variability of representation error and the influence of various factors in creating this variability are examined here. The larger the variations that are caused due to sub-grid processes within the grid  
440 box of 1° × 1°, the larger the representation error. The derived seasonal differences in structural patterns of the sub-grid variability facilitate to 1) quantify what would be typical representation errors associated with incorporating observations from different seasons into atmospheric models 2) determine what drives the

seasonality in sub-grid variability and ultimately 3) design a possible parameterization of representation error with a seasonal component in the inverse modelling framework as well as identify periods or seasons where the use of this parameterization would be valid to improve our estimations of CO<sub>2</sub> fluxes. Further, the seasonal  
445 spatial variability analysis of column averages can provide useful information to gap-fill the satellite-based products over India when large data gaps are present, which can be utilized for applications that do not demand high precision observations (e.g. Hammerling et al., 2012).

### 3.2.1 Spatio-temporal patterns

Representation errors in the surface CO<sub>2</sub> concentrations of a global model at a spatial resolution of 1° × 1° for  
450 July and November are shown in Fig. 4. The representation error at 1° × 1° spatial scale reaches values ranging from 0.5 ppm to 5 ppm, which are comparable to the magnitude of variability at hotspot emission regions or half of the seasonal variability of CO<sub>2</sub> over the region (see Fig. 2b). The median representation error is 1.2 ppm at the surface, which is considerably larger than the measurement errors. In the case of high accuracy in situ measurements, the typical uncertainty for CO<sub>2</sub> measurements is of the order of 0.1 ppm (Andrews et al., 2014,  
455 Zellweger et al., 2016). A remarkable feature is the presence of very high representation error over North-East and Western Ghats regions, where the biosphere activity is very prominent. The heterogeneous distribution of biosphere fluxes generates significant sub-grid scale variability that leads to high representation error. Also, we can find high representation error along the foothills of the Himalayas. In addition to the complex terrain, the region over the Ganges basin is characterized by increased anthropogenic activity, which contributes to a larger  
460 representation error surrounding this region. High representation error is also found in the coastal regions, ranging from 2 ppm to 5 ppm (median of 4 ppm) due to the temporal covariance between the coastal meteorology and exchange fluxes. The CO<sub>2</sub> fluxes from coastal regions can be transported over the ocean and accumulated in the shallow boundary layer over the ocean. The shallow boundary layer is a characteristic of the marine atmosphere due to the less vertical mixing compared to land regions. Horizontal CO<sub>2</sub> gradients can also  
465 be generated by the influence of highly varying biospheric fluxes under different advection patterns at the boundary between land and ocean. A similar mechanism is applicable to mountain regions where temporal covariance of mountain-valley circulation and respired CO<sub>2</sub> fluxes are regulated by atmospheric radiation. The terrain-following coordinates as used in the model may also result in spurious tracer concentration gradients over the steep mountain terrain (Beck et al., 2020; Skamarock et al., 2021; Park et al., 2019). Though the  
470 mesoscale models are expected to perform better in simulating CO<sub>2</sub> variations over the complex terrain than the coarse models (e.g. Engelen et al., 2002; Gerbig et al., 2003; Ahmadov et al., 2007; Corbin et al., 2008; Lauvaux et al., 2009b; Pillai et al., 2011; Uebel et al., 2017; Agustí-Panareda et al., 2019), they may also suffer from the inadequate representation of complex weather features and associated variability. We can also find individual cells with high representation errors associated with point emission sources such as cities, mining sites, and  
475 coal-fired power plants at different parts of the domain. The daily variations in surface representation errors are small within a month, although there exists a clear distinction between daytime and nighttime values (Figure not shown). The nighttime representation error is higher (e.g. a median value of 1.5 ppm for surface during November) compared to the daytime representation error (e.g. a median value of 1.1 ppm for surface during November) throughout the analysed domain. This is expected due to the coupling between nocturnal shallow  
480 transport and different flux processes accentuating local effects. During the nighttime, photosynthesis is absent,

and respiration is the major biospheric activity, leading to an increase in CO<sub>2</sub> concentration in the atmosphere. The large heterogeneity in flux distribution that is mostly from respired CO<sub>2</sub> fluxes, the shallow boundary layer processes and the weak nocturnal turbulence cause CO<sub>2</sub> to be accumulated locally near the surface with large variations. Compared to July, we find higher representation error in November owing to the wintertime transport with decreased vertical mixing and heterogeneous biospheric uptake (see Fig. 4).

In the case of XCO<sub>2</sub>, the magnitude of sub-grid scale variability is much smaller than that of surface CO<sub>2</sub> (Fig. 5), but it follows a similar spatial pattern. This confirms the dominance of surface-level processes in causing sub-grid variability of column averages. The sub-grid scale variability in XCO<sub>2</sub> reaches up to 2 ppm in some parts of the region, especially where there are high variations in topographic features or point emission sources. The estimated column representation errors over these regions are thus capable of causing significant biases in the satellite inferred CO<sub>2</sub> fluxes as regional biases of a few tenths of parts per million in column-averaged CO<sub>2</sub> can create a bias of a few tenths of a gigaton of carbon fluxes (Chevallier et al., 2007). Also, the representation error for a large part of the domain is found to be above 0.5 ppm, which is around half of the typical precision of current satellite measurements. Note that the representation error reported here is different from satellite measurement errors (e.g. spectroscopic retrieval error or sampling biases) and tends to be systematic in nature.

Figure 6 shows the statistical distribution of the representation error ( $\sigma_{CO_2}$ ) sampled over India, during July and November, separated by daytime and nighttime. July shows a median surface representation error of 0.9 ppm and 1.1 ppm during daytime and nighttime respectively, while November shows a median value of 1.1 ppm and 1.4 ppm for daytime and nighttime respectively. In July, 95 % of the representation error is less than 2.1 ppm for daytime (3.9 ppm for nighttime) while it is 3 ppm for daytime (4.2 ppm for nighttime) for November. For column average, median values for representation error are 0.3 ppm and 0.4 ppm for July daytime and November daytime respectively.

To further reduce the effect of random error that might be introduced by short-term weather phenomena, the representation errors ( $\sigma_{\overline{CO_2}_{(mon)}}$ ) are calculated from the monthly averaged CO<sub>2</sub> field and are denoted as a systematic error (Fig. 6). Uncorrelated errors are expected to decrease when averaging over a sufficiently long period. As expected, the median values of the systematic representation errors are smaller for all cases, showing the effect of random errors. Especially for November when the cyclonic event was present, the values of the systematic errors (in the 95% percentile) for the surface CO<sub>2</sub> are considerably lower than total errors, reducing from 3 ppm (daytime) and 4.2 ppm (nighttime) to 2.2 ppm (daytime) and 3 ppm (nighttime). In the case of column CO<sub>2</sub>, this reduction is from 1.1 ppm (daytime) and 0.9 ppm (nighttime) to 0.8 ppm (daytime) and 0.7 ppm (nighttime) in the 95% percentile. In contrast to surface representation error (Fig. 6a), median values of nighttime representation errors are found to be slightly lower than daytime representation error for column average (Fig. 6b). To assess the dependence of representation error on possible horizontal resolutions of the global models, we have further derived the representation errors for different spatial resolutions between 0.5° and 4°. As expected, we see reductions in representation errors for both surface and column averaged CO<sub>2</sub> with increasing horizontal resolution of the model (See Fig. 7 & supplementary Fig. S4). During July, the median surface representation error reduced from 1.6 ppm (2 ppm) to 0.6 ppm (0.7 ppm) during daytime (nighttime) while increasing horizontal resolution from 4° to 0.5°. This increment in spatial resolution has also resulted in

520 similar error reductions in November during which the median of surface representation error shows a reduction  
from 2.4 ppm (2.8 ppm) to 0.7 ppm (0.9 ppm) during daytime (nighttime). In the case of column-averaged  
values, the median representation error decreased from 0.7 ppm (0.6 ppm) to 0.25 ppm (0.2 ppm) during July  
daytime (nighttime) and from 0.95 ppm (0.9 ppm) to 0.25 ppm (0.2 ppm) during November daytime  
(nighttime). The spatial distribution of representation errors for a model with a horizontal grid resolution of  
525  $0.5^\circ \times 0.5^\circ$  (e.g. regional models) is provided in Supplementary Figs. S5 and S6. On average, we find ~33 to 36  
% of decrease in daytime representation errors for both months when increasing model grid resolution from  $1^\circ$   
to  $0.5^\circ$ . There exists a similar spatial pattern of representation errors for both resolutions of  $0.5^\circ$  and  $1^\circ$ . Though  
our results indicate a reduction of representation error for regional models with a typical resolution of  $0.5^\circ$   
compared to global models with  $1^\circ$  spatial resolution, the emission hotspots and point sources are still  
pronounced with high sub-grid scale variability, especially during nighttime. The above analyses indicate that  
530 the sub-grid variability alone can produce significantly higher errors compared to the measurement errors (e.g.,  
0.1 ppm as per WMO standards for surface measurements), which necessitates a proper treatment of these errors  
in models for the optimal estimation of CO<sub>2</sub> fluxes.

### 3.2.2 Vertical distribution

535 Figure 8 shows the vertical profile of representation error distribution within different altitude bins. We find that  
the maximum representation error is in the surface layer, and most of the higher values are found to be within  
the lowest 4-6 km bins. Also, sub-grid scale variability decreases sharply with increasing altitude. This  
dominance of variability in surface concentration can be explained by surface flux heterogeneity influencing  
mole fractions in lower atmospheric layers (PBL) as described in van der Molen and Dolman (2007) and Pillai  
et al. (2010). There is a slight increase in representation error in the upper tropospheric levels near 12 to 14 km  
540 altitude range. This may be associated with the presence of strong circulations in the upper troposphere and  
lower stratosphere, such as subtropical westerly jets or Asian summer monsoon anticyclone (e.g. Chandra et al.,  
2017).

### 3.3. Influence of terrain heterogeneity and flux variability on representation errors

545 Here we explore the factors influencing the size and patterns of the representation error in coarse models. For  
this, statistical relationships between representation error and possible explanatory variables are examined for  
both surface and column-averaged CO<sub>2</sub>. Identifying these factors influencing representation errors and  
quantifying their local effects facilitate us to further investigate on how these biases in retrieved fluxes can be  
minimized in global models (see Sect. 3.5).

550 We find a significant influence of terrain heterogeneity on representation error, which is evident from the spatial  
maps in Figs. 4 and 5, where the largest sub-grid scale variations are found in the Himalayan regions. Spatial  
variations in topography produce mesoscale circulation patterns and corresponding variations in atmospheric  
CO<sub>2</sub> at fine scales. At the same time, there is a plausible additional error in global model simulations related to  
the insufficient resolution of vertical grids necessary to account for different surface influences (e.g. mountain  
vs valley). This effect of coarse vertical resolution is excluded in our representation error estimates by  
555 preserving the vertical grids used for the high-resolution simulations. To further explore the importance of using  
the high-resolution topography data on representing the CO<sub>2</sub> variability, we analyse the dependence of terrain

variations (as derived from the standard deviation of terrain height) on the distribution of the representation error. We have estimated the statistical dependence ( $R^2$ ) of representation error on topographic variability within the corresponding global climate models' grids to understand the relation between them. Topographic variability within  $1^\circ \times 1^\circ$  spatial box is estimated as the standard deviation of topography (m) for all  $10 \text{ km} \times 10 \text{ km}$  boxes within the larger grid, and is denoted as  $\sigma_{topo}$ . Bins are created based on the values of this topographic variability, in which different points from different parts of the domain are binned together on the basis of their standard deviation of topography. Each bin is created with a size of 50 m variation in terrain height. The linear fit is estimated between the average value of topographic variability within a bin and the average value of representation error of the corresponding points in the bin. Our results show that the terrain heterogeneity alone can explain about 20-48% ( $R^2 = 0.20$  to  $0.40$ ) of the surface representation errors over the domain. In a similar way, we have estimated the influence of topographic variability on representation error in the column-averaged model simulations. It is found that topography alone can explain 45-52 % ( $R^2 = 0.45$  to  $0.52$ ) of representation errors in the column-averaged simulations.

Further, we estimate the statistical relationship ( $R^2$ ) between the surface flux heterogeneity and representation error. The surface representation error is strongly linked to the biosphere flux variability, and the relationship between heterogeneity in biospheric surface flux (as derived from the standard deviation of VPRM-derived NEE fluxes, denoted as  $\sigma_{bio}$ ) and representation errors depends on the time of the day and season. During daytime when there is strong ecosystem activity, the dependence of representation error ( $\sigma_{CO_2}$ ) on  $\sigma_{bio}$  of surface and column  $CO_2$  is found to be ~75-80 % and ~66-74 % respectively.  $\sigma_{bio}$  explains about 62% for the surface  $CO_2$  variability and 48 % for the column variability during July nighttime. However,  $\sigma_{CO_2}$  and  $\sigma_{bio}$  are less correlated (23 % for surface and 19 % for column) during November nighttime. The diurnal difference in the dependence of representation error on  $\sigma_{bio}$  can be explained by the increased magnitude and spatial variability of daytime biospheric fluxes in the growing season (primarily due to photosynthesis activities) compared to nighttime fluxes. Moreover, poor vertical mixing under the stable nocturnal atmospheric conditions with more advection and drainage flow reduces the influence of surface fluxes on spatial variability of mixing ratios. The dependence of representation error on the anthropogenic flux heterogeneity (as derived from the standard deviation of EDGAR fluxes, denoted as  $\sigma_{ant}$ ) is found to be negligible except for nighttime (13–30 %). We find less influence of seasonality on the relationship between anthropogenic surface flux heterogeneity and representation errors (see Supplementary Table S1). Similar to the above analysis with  $\sigma_{bio}$ , the combined effect of atmospheric stability and flux heterogeneity can explain the diurnal differences of the relationship between  $\sigma_{ant}$  and  $\sigma_{CO_2}$ .

In case of the variability of monthly averages, we see that  $\sigma_{\overline{CO_2}(mon)}$  is well explained by  $\sigma_{bio}$  during daytime (see Supplementary Table S2), as expected. A similar strong correlation can be seen between  $\sigma_{\overline{CO_2}(mon)}$  and  $\sigma_{bio}$  (23–69 %) during nighttime for surface variability of  $CO_2$ , while there exists only less dependence of nocturnal column  $CO_2$  variability on local fluxes. This shows the decoupling of the mixing ratios in other parts of the column from the surface during the night due to less vertical mixing, combined with more drainage flow

in the nocturnal boundary layer, which reduces the effect of surface flux variability on the column CO<sub>2</sub> variability.

595 In general, the above analysis underlines the need for using Digital Elevation Models (DEMs) at high resolution to take into account the terrain-induced mesoscale atmospheric flows adequately in atmospheric transport models. Further, the results indicate the importance of utilising high-resolution surface fluxes in atmospheric CO<sub>2</sub> simulations.

### 3.4 Estimation of NEE flux uncertainty due to representation error

600 By following the assumptions and approach as given in Sect. 2.4, we have estimated the NEE flux uncertainty resulting from the representation errors. The results based on the OSSEs for nine observation sites are given in Table. 3. The scaling factors, which are calculated separately for each site by adjusting the prior fluxes using pseudo-observations, are applied to the VPRM monthly fluxes. The total NEE flux for India estimated by VPRM for July and November are -373.3 MtCO<sub>2</sub> per month and -417.1 MtCO<sub>2</sub> per month, respectively. The  
605 flux uncertainties over India that arise solely due to the contribution from the representation error are estimated to be 38.59 (daytime observations) to 30.14 (nighttime observations) MtCO<sub>2</sub> per month (10.33% to 8.07%) for July and 18.42 (daytime observations) to 13.34 (nighttime observations) MtCO<sub>2</sub> per month (4.4% to 3.1%) for November while utilizing data from nine observation stations. The spatial representativeness of measurement stations used in this study is assumed to cover only 35% of the country's total area (see Sect. 2.4). Consequently,  
610 the impact of representation error on flux uncertainty, as reported in this study, is an underestimation when measurements from more regionally representative sites or a dense observation network are utilized in inversions. The maximum flux uncertainty was found for July due to the enhanced biosphere activity and unresolved convection activities. The estimated uncertainties are considerable for the carbon budget assessment especially given that these errors arise solely from the global models' representation error. Note that calculated  
615 representation error does not include other transport error sources such as advection, convection or vertical mixing.

### 3.5 Possible treatment of representation error in the global model

The simplest possible way to minimize the uncertainty in flux estimation using a coarse model is to construct a parameterization model that can account for the representation error using explanatory variables. For this, we  
620 create a multivariate model to capture spatial patterns in the representation error. Employing this parameterization in a global model would thus redefine the likelihood of better estimates (improving the state of knowledge) with variance greater than that of the measurement error in the inverse framework by minimizing the modelling error. The multivariate linear model with explanatory variables that include sub-grid variations of terrain ( $\sigma_{topo}$ ), biospheric ( $\sigma_{bio}$ ) and anthropogenic ( $\sigma_{ant}$ ) fluxes remarkably captures the derived column  
625 representation error all over the Indian region during July daytime with a R<sup>2</sup> value of 0.96 (Fig. 9). The difference between the modelled and derived representation error is found to be well below 0.5 ppm in most parts of the domain. Similarly, we have modelled the surface representation error using the linear model with these three explanatory variables and found that the proposed model could capture the derived surface representation error well (R<sup>2</sup> = 0.89) with a deviation less than 1 ppm in most of the regions (see Supplementary  
630 Fig. S7 and Supplementary Table S1 and S2). More work is needed to demonstrate the extent of applicability of

this method to minimize the flux uncertainties while utilizing actual observations. Nevertheless, the above finding provides a possibility for a parameterization that can be further developed in inverse models or data assimilation systems, which defines the degrees of freedom for describing the posterior states. Applying this parameterization scheme to the specific problem requires a high-resolution map of the terrain and prior information on anthropogenic and biogenic fluxes as the uncertainties in the topography and surface fluxes can significantly impact flux estimation. The caveat of this linear model is that the uncorrelated spatial variability in the prior and true states of the fluxes is ignored in the present form, which cannot be the case for the real inverse problems. This assumption obviously hampers the system in achieving the maximum reduction in uncertainty, and further study is needed to refine this model from a practical perspective. We emphasise, however, that the above parameterization does not require a high-resolution simulation of transport, which has high computational costs.

#### 4. Conclusion

Given the upcoming availability of atmospheric observations over India, significant effort is required to critically enhance the modelling capabilities to derive carbon budgets over India within the definite confidence intervals and at scales relevant to the ecosystem and countrywide policy-making. The misrepresentation of mesoscale transport phenomena and unresolved flux variations in modelling systems operating on coarse grids hinders the optimal utilization of observations. In this context, the present study quantifies the spatial variability of atmospheric CO<sub>2</sub> mixing ratio over India that is not resolved by the coarse models and assesses their impact on flux estimations. We demonstrate the potential of a simple parameterization scheme to model these unresolved variations in the coarse models for minimizing the uncertainty in retrieved fluxes.

A large spread among existing global model simulations in representing monthly averaged CO<sub>2</sub> concentration profiles indicates a considerable knowledge gap in the estimations of fluxes even at a monthly scale. It can be argued that a significant part of these differences arises due to the lack of observational constraints over India, which leads to a possible compensatory model artefact over this region in order to match the global mass constraint. At the same time, it is also expected that the spatial variability of the observed atmospheric CO<sub>2</sub> mole fractions can be large so that these coarse models fail to represent them adequately. For instance, we find that the unresolved variations (representation error) of global models with a spatial resolution of 1° × 1° can be ~1.5 ppm on average for the surface CO<sub>2</sub> that is even larger than the currently reported differences between global models (~1 ppm). Similarly, the average representation error estimated for the column-averaged CO<sub>2</sub> is ~1.1 ppm. These estimated values are larger than the corresponding measurement errors, which cause the inverse optimization to infer a state that is not close to the truth as is required in the regional CO<sub>2</sub> budget for various applications.

Coastal areas and mountains have particularly high representation errors (≈4 ppm for surface CO<sub>2</sub>). Emission hotspots can also lead to significant CO<sub>2</sub> variability near the surface as large as ≈8 ppm. Larger values are typically associated with the nocturnal shallow boundary layer dynamics and the stronger respiration signal with considerable flux variability. These findings are consistent with Pillai et al. (2010), which show that there exist spatial differences in the sub-grid variability for both surface and column CO<sub>2</sub>. Although the magnitude of the sub-grid variability of the total column is significantly smaller than the variability at the surface, the spatial

670 pattern remains similar for both, owing to the dominance of surface heterogeneity in topography and fluxes.  
675 With the underlying assumptions, the total uncertainty in optimized fluxes solely due to the unresolved sub-grid  
680 variations is estimated to be 3.1 to 10.3% of the total NEE while utilizing pseudo-data from nine observation  
stations over India. Increasing the spatial and temporal resolutions of the transport models can generally capture  
the mesoscale features and associated CO<sub>2</sub> gradients, thereby reducing the representation error. Increasing the  
model's resolution from 1° to 0.5° has shown an improvement in capturing variability with representation error  
reduction of 33% and 36% for summer time and winter time, respectively. By showing the existence of  
unresolved variability in 0.5° resolution with a similar spatial pattern of error as of 1° spatial resolution, we  
demonstrate the need for a much finer resolution than 0.5° for representing the atmospheric CO<sub>2</sub> variability over  
India. However, merely increasing the resolution without having a realistic representation of terrain  
heterogeneity and flux (both natural and anthropogenic) variability would not be beneficial. The uncertainties in  
the high-resolution fluxes can worsen the model's skills, whose effect would not be more pronounced at coarser  
resolutions due to the diffusive nature of fluxes, as seen in Agustí-Panareda et al. (2019).

685 A parameterization scheme with explanatory variables of sub-grid variations of terrain, biospheric and  
anthropogenic fluxes is shown to capture a considerable fraction of expected representation error in the global  
model. The proposed method is easy to implement in the coarse models as it does not require computationally  
expensive transport simulations at high resolution. As we see a significant dependence of the distribution of sub-  
grid variability on terrain variations, our results reinforce the requirement for using high-resolution DEMs in the  
atmospheric transport models. The biosphere flux variability explains about 62 to 80% of the surface  
representation errors over the Indian region, indicating the need for using precise high-resolution surface fluxes.

690 Overall, we show that the mesoscale transport mechanisms and flux variability contribute to fine-scale CO<sub>2</sub>  
variations that the current-generation models cannot resolve. Our findings indicate that the models need to be  
critically improved to capture mesoscale variations associated with horizontal and vertical transport and fine-  
scale flux variability to maximize the potential of highly precise and accurate measurements. Our results provide  
a baseline for overcoming the shortcomings mentioned above and accounting for the realistic distribution of  
atmospheric CO<sub>2</sub> to improve the estimation of surface fluxes through inverse modelling.

695

#### **Code/Data availability**

The WRF-Chem source code is publicly available at <https://ruc.noaa.gov/wrf/wrf-chem/> (last access: 10 August 2019). The CarbonTracker (CT-2019B) products are available online at <http://carbontracker.noaa.gov> (last access: 21 July 2020, Jacobson et al., 2020). The data from the CarboScope inversion system are available  
700 online at <http://www.bgc-jena.mpg.de/CarboScope/> (last access: 20 July 2020, Rödenbeck et al., 2003). The data  
from the LSCE modelling system used in this study are available at <http://atmosphere.copernicus.eu> (last access:  
22 July 2020, Chevallier et al., 2019). The sub-grid variability products based on the WRF-GHG model  
simulations can be accessed from <https://zenodo.org/record/6616466> (last access: 23 May 2022, Thilakan and  
Pillai, 2022). The WRF-GHG model CO<sub>2</sub> simulations used for this study are available upon request to the  
705 corresponding author, Dhanyalekshmi Pillai (dhanya@iiserb.ac.in, kdhanya@bgc-jena.mpg.de). The EDGAR  
data used in this study are publicly available at <https://edgar.jrc.ec.europa.eu/> (last access: 15 March 2020,  
Crippa et al., 2018). The GFAS data are publicly available at <http://apps.ecmwf.int/datasets/data/cams-gfas/> (last

access: 15 March 2020, Kaiser et al., 2012). The ERA5 data are available at <https://cds.climate.copernicus.eu/cdsapp#!/home> (last access: 18 March 2020, Hersbach et al., (2020)).

## 710 **Author Contribution**

DP designed the study and performed the model simulations. VT performed the analysis and wrote the paper. VT and DP interpreted the results. CG, MG, AR and TAM provided significant input to the interpretation, and the improvement of the paper. All authors discussed the results and commented on the paper.

## **Competing interests**

715 The authors declare they have no conflict of interest.

## **Acknowledgements**

This study is supported by the funding from the Max Planck Society allocated to the Max Planck Partner Group at IISERB and the Science and Engineering Research Board (SERB) through Early Career Research Award (ECR/2018/001111) to DP. TAM acknowledges the financial support provided by SERB grant (Junior Research  
720 Fellowship). We acknowledge the support of IISERB's high performance cluster system for computations, data analysis and visualisation. The WRF-Chem simulations were done on the high-performance cluster Mistral of the Deutsches Klimarechenzentrum GmbH (DKRZ). We thank the Editor and both referees for their constructive comments.

## 725 **References**

- Agustí-Panareda, A., Diamantakis, M., Massart, S., Chevallier, F., Muñoz-Sabater, J., Barré, J., Curcoll, R., Engelen, R., Langerock, B., Law, R. M., Loh, Z., Morguí, J. A., Parrington, M., Peuch, V.-H., Ramonet, M., Roehl, C., Vermeulen, A. T., Warneke, T., and Wunch, D.: Modelling CO<sub>2</sub> weather – why horizontal resolution matters, *Atmospheric Chemistry and Physics*, 19, 7347–7376,  
730 <https://doi.org/10.5194/acp-19-7347-2019>, 2019.
- Ahmadov, R., Gerbig, C., Kretschmer, R., Koerner, S., Neining, B., Dolman, A. J., and Sarrat, C.: Mesoscale covariance of transport and CO<sub>2</sub> fluxes: Evidence from observations and simulations using the WRF-VPRM coupled atmosphere-biosphere model, *Journal of Geophysical Research*, 112, D22107, <https://doi.org/10.1029/2007jd008552>, 2007.
- 735 Ahmadov, R., Gerbig, C., Kretschmer, R., Körner, S., Rödenbeck, C., Bousquet, P., and Ramonet, M.: Comparing high resolution WRF-VPRM simulations and two global CO<sub>2</sub> transport models with coastal tower measurements of CO<sub>2</sub>, *Biogeosciences*, 6, 807–817, <https://doi.org/10.5194/bg-6-807-2009>, 2009.
- Ahmadov, R., McKeen, S. A., Robinson, A. L., Bahreini, R., Middlebrook, A. M., de Gouw, J. A., Meagher, J.,  
740 E.-Y., Edgerton, E., Shaw, S., and Trainer, M.: A volatility basis set model for summertime secondary organic aerosols over the eastern United States in 2006, *Journal of Geophysical Research: Atmospheres*, 117, D06301, <https://doi.org/10.1029/2011JD016831>, 2012.
- Andrews, A. E., Kofler, J. D., Trudeau, M. E., Williams, J. C., Neff, D. H., Masarie, K. A., Chao, D. Y., Kitzis, D. R., Novelli, P. C., Zhao, C. L., Dlugokencky, E. J., Lang, P. M., Crotwell, M. J., Fischer, M. L.,

- 745 Parker, M. J., Lee, J. T., Baumann, D. D., Desai, A. R., Stanier, C. O., De Wekker, S. F. J., Wolfe, D. E., Munger, J. W., and Tans, P. P.: CO<sub>2</sub>, CO, and CH<sub>4</sub> measurements from tall towers in the NOAA Earth System Research Laboratory's Global Greenhouse Gas Reference Network: instrumentation, uncertainty analysis, and recommendations for future high-accuracy greenhouse gas monitoring efforts, *Atmospheric Measurement Techniques*, 7, 647–687, <https://doi.org/10.5194/amt-7-647-2014>, 2014.
- 750 Beck, V., Koch, T., Kretschmer, R., Marshall, J., Ahmadov, R., Gerbig, C., Pillai, D., and Heimann, M.: The WRF Greenhouse Gas Model (WRF-GHG), Tech. Rep. 25, Max Planck Institute for Biogeochemistry, Jena, Germany, 2011.
- Beck, J., Brown, J., Dudhia, J., Gill, D., Hertnecky, T., Klemp, J., Wang, W., Williams, C., Hu, M., James, E., Kenyon, J., Smirnova, T., & Kim, J.: An Evaluation of a Hybrid, Terrain-Following Vertical Coordinate in the WRF-Based RAP and HRRR Models, *Weather and Forecasting*, 35(3), 1081-1096, <https://doi.org/10.1175/WAF-D-19-0146.1>, 2020.
- 755 Bergamaschi, P., Danila, A., Weiss, R. F., Ciais, P., Thompson, R. L., Brunner, D., Levin, I., Meijer, Y., Chevallier, F., Bovensmann, H., Crisp, D., Basu, S., Dlugokencky, E., Engelen, R., Gerbig, C., Günther, D., Hammer, S., Henne, S., Houweling, S., Peylin, P., Pinty, B., Ramonet, M., Reimann, S., Röckmann, T., Schmidt, M., Strogies, M., Sussams, J., Tarasova, O., van Aardenne, J., Vermeulen, A. T., and Vogel, F.: Atmospheric monitoring and inverse modelling for verification of greenhouse gas inventories, Publications Office of the European Union, 2018.
- 760 Bousquet, P., Peylin, P., Ciais, P., Le Quéré, C., Friedlingstein, P., and Tans, P. P.: Regional Changes in Carbon Dioxide Fluxes of Land and Oceans Since 1980, *Science*, 290, 1342–1346, <https://doi.org/10.1126/science.290.5495.1342>, 2000.
- 765 Bréon, F. M., Broquet, G., Puygrenier, V., Chevallier, F., Xueref-Remy, I., Ramonet, M., Dieudonné, E., Lopez, M. and Schmidt, M., Perrussel, O., and Ciais, P.: An attempt at estimating Paris area CO<sub>2</sub> emissions from atmospheric concentration measurements, *Atmospheric Chemistry and Physics*, 15, 1707–1724, <https://doi.org/10.5194/acp-15-1707-2015>, 2015.
- 770 Broquet, G., Chevallier, F., Bréon, F.-M., Kadyrov, N., Alemanno, M., Apadula, F., Hammer, S., Haszpra, L., Meinhardt, F., Morguí, J. A., Necki, J., Piacentino, S., Ramonet, M., Schmidt, M., Thompson, R. L., Vermeulen, A. T., Yver, C., and Ciais, P.: Regional inversion of CO<sub>2</sub> ecosystem fluxes from atmospheric measurements: reliability of the uncertainty estimates, *Atmospheric Chemistry and Physics*, 13, 9039–9056, <https://doi.org/10.5194/acp-13-9039-2013>, 2013.
- 775 Carouge, C., Bousquet, P., Peylin, P., Rayner, P. J., and Ciais, P.: What can we learn from European continuous atmospheric CO<sub>2</sub> measurements to quantify regional fluxes – Part 1: Potential of the 2001 network, *Atmospheric Chemistry and Physics*, 10, 3107–3117, <https://doi.org/10.5194/acp-10-3107-2010>, 2010.
- Cervarich, M., Shu, S., Jain, A. K., Arneeth, A., Canadell, J., Friedlingstein, P., Houghton, R. A., Kato, E., Koven, C., Patra, P., Poulter, B., Sitch, S., Stocker, B., Viovy, N., Wiltshire, A., and Zeng, N.: The terrestrial carbon budget of South and Southeast Asia, *Environmental Research Letters*, 11, 105006, <https://doi.org/10.1088/1748-9326/11/10/105006>, 2016.
- 780 Chandra, N., Hayashida, S., Saeki, T., and Patra, P. K.: What controls the seasonal cycle of columnar methane observed by GOSAT over different regions in India?, *Atmos. Chem. Phys.*, 17, 12633–12643, <https://doi.org/10.5194/acp-17-12633-2017>, 2017.

- 785 Chen, H. W., Zhang, L. N., Zhang, F., Davis, K. J., Lauvaux, T., Pal, S., Gaudet, B., and DiGangi, J. P.: Evaluation of Regional CO<sub>2</sub> Mole Fractions in the ECMWF CAMS Real-Time Atmospheric Analysis and NOAA CarbonTracker Near-Real-Time Reanalysis with Airborne Observations from ACT-America Field Campaigns, *Journal of Geophysical Research: Atmospheres*, 124, 8119–8133, <https://doi.org/10.1029/2018jd029992>, 2019.
- 790 Chevallier, F., Fisher, M., Peylin, P., Serrar, S., Bousquet, P., Bréon, F.-M., Chédin, A., and Ciais, P.: Inferring CO<sub>2</sub> sources and sinks from satellite observations: Method and application to TOVS data, *Journal of Geophysical Research*, 110, D24309, <https://doi.org/10.1029/2005jd006390>, 2005.
- Chevallier, F., Bréon, F. M., and Rayner, P. J.: Contribution of the Orbiting Carbon Observatory to the estimation of CO<sub>2</sub> sources and sinks: Theoretical study in a variational data assimilation framework, *Journal of Geophysical Research*, 112, D09307, <https://doi.org/10.1029/2006JD007375>, 2007.
- 795 Chevallier, F., Ciais, P., Conway, T. J., Aalto, T., Anderson, B. E., Bousquet, P., Brunke, E. G., Ciattaglia, L., Esaki, Y., Fröhlich, M., Gomez, A., Gomez-Pelaez, A. J., Haszpra, L., Krummel, P. B., Langenfelds, R. L., Leuenberger, M., Machida, T., Maignan, F., Matsueda, H., Morguá, J. A., Mukai, H., Nakazawa, T., Peylin, P., Ramonet, M., Rivier, L., Sawa, Y., Schmidt, M., Steele, L. P., Vay, S. A., Vermeulen, A. T., Wofsy, S., and Worthy, D.: CO<sub>2</sub> surface fluxes at grid point scale estimated from a global 21 year reanalysis of atmospheric measurements, *Journal of Geophysical Research*, 115, D21307, <https://doi.org/10.1029/2010jd013887>, 2010.
- 800 Chevallier, F.: On the parallelization of atmospheric inversions of CO<sub>2</sub> surface fluxes within a variational framework, *Geoscientific Model Development*, 6, 783–790, <https://doi.org/10.5194/gmd-6-783-2013>, 2013.
- 805 Chevallier, F., Remaud, M., O'Dell, C. W., Baker, D., Peylin, P., and Cozic, A.: Objective evaluation of surface- and satellite-driven carbon dioxide atmospheric inversions, *Atmospheric Chemistry and Physics*, 19, 14233–14251, <https://doi.org/10.5194/acp-19-14233-2019>, 2019.
- 810 Ciais, P., Dolman, A. J., Bombelli, A., Duren, R., Peregón, A., Rayner, P. J., Miller, C., Gobron, N., Kirdnerman, G., Marland, G., Gruber, N., Chevallier, F., Andres, R. J., Balsamo, G., Bopp, L., Bréon, F.-M., Broquet, G., Dargaville, R., Battin, T. J., Borges, A., Bovensmann, H., Buchwitz, M., Butler, J., Canadell, J. G., Cook, R. B., DeFries, R., Engelen, R., Gurney, K. R., Heinze, C., Heimann, M., Held, A., Henry, M., Law, B., Luysaert, S., Miller, J., Moriyama, T., Moulin, C., Myneni, R. B., Nussli, C., Obersteiner, M., Ojima, D., Pan, Y., Paris, J.-D., Piao, S. L., Poulter, B., Plummer, S., Quegan, S., Raymond, P., Reichstein, M., Rivier, L., Sabine, C., Schimel, D., Tarasova, O., Valentini, R., Wang, R., van der Werf, G., Wickland, D., Williams, M., and Zehner, C.: Current systematic carbon-cycle observations and the need for implementing a policy-relevant carbon observing system, *Biogeosciences*, 11, 3547–3602, <https://doi.org/10.5194/bg-11-3547-2014>, 2014.
- 815 Corbin, K. D., Denning, A. S., Lu, L., Wang, J.-W., and Baker, I. T.: Possible representation errors in inversions of satellite CO<sub>2</sub> retrievals, *Journal of Geophysical Research*, 113, D02301, doi:10.1029/2007JD008716, 2008.
- 820 Crippa, M., Guizzardi, D., Muntean, M., Schaaf, E., Dentener, F., van Aardenne, J. A., Monni, S., Doering, U., Olivier, J. G. J., Pagliari, V., and Janssens-Maenhout, G.: Gridded emissions of air pollutants for the

- 825 period 1970–2012 within EDGAR v4.3.2, *Earth System Science Data*, 10, 1987–2013, <https://doi.org/10.5194/essd-10-1987-2018>, 2018.
- Crippa, M., Guizzardi, D., Muntean, M., Schaaf, E., Lo Vullo, E., Solazzo, E., Monforti-Ferrario, F., Olivier, J., Vignati, E.: EDGAR v6.0 Greenhouse Gas Emissions. European Commission, Joint Research Centre (JRC) [Dataset] PID: <http://data.europa.eu/89h/97a67d67-c62e-4826-b873-9d972c4f670b>, 2021.
- 830 Department of Agriculture & Cooperation, Ministry of Agriculture (DAC/MA): Agricultural Statistics at a Glance 2014, Directorate of Economics and Statistics, Department of Agriculture and Cooperation (DAC), Ministry of Agriculture (MA), Government of India, OUP, New Delhi, India, ISBN 0-19-945965-7, available at: <https://eands.dacnet.nic.in/PDF/Agricultural-Statistics-At-Glance2014.pdf> (last access: 11 February 2021), 2015.
- 835 Denvil-Sommer, A., Gehlen, M., Vrac, M., and Mejia, C.: LSCE-FFNN-v1: a two-step neural network model for the reconstruction of surface ocean pCO<sub>2</sub> over the global ocean, *Geoscientific Model Development*, 12, 2091–2105, <https://doi.org/10.5194/gmd-12-2091-2019>, 2019.
- Engelen, R. J., Denning, A. S., Gurney, K. R., and TransCom3 modelers: On error estimation in atmospheric CO<sub>2</sub> inversions, *Journal of Geophysical Research*, 107, 4635, doi:10.1029/2002JD002195, 2002.
- 840 Enting, I. G.: *Inverse Problems in Atmospheric Constituent Transport*, Cambridge Atmospheric and Space Science Series, Cambridge University Press, <https://doi.org/10.1017/CBO9780511535741>, 2002.
- Friedlingstein, P., Jones, M. W., O’Sullivan, M., Andrew, R. M., Hauck, J., Peters, G. P., Peters, W., Pongratz, J., Sitc h, S., Le Quéré, C., Bakker, D. C. E., Canadell, J. G., Ciais, P., Jackson, R. B., Anthoni, P., Barbero, L., Bastos, A., Bas trikov, V., Becker, M., Bopp, L., Buitenhuis, E., Chandra, N., Chevallier, F., Chini, L. P., Currie, K. I., Feely, R. A., Gehlen, M., Gilfillan, D., Gkritzalis, T., Goll, D. S., Gruber, N., Gutekunst, S., Harris, I., Haverd, V., Houghton, R. A., Hurtt, G., Ilyina, T., Jain, A. K., Joetzjer, E., Kaplan, J. O., Kato, E., Klein Goldewijk, K., Korsbakken, J. I., Landschützer, P., Lau vset, S. K., Lefèvre, N., Lenton, A., Lienert, S., Lombardozzi, D., Marland, G., McGuire, P. C., Melton, J. R., Metzl, N., Mun ro, D. R., Nabel, J. E. M. S., Nakaoka, S.-I., Neill, C., Omar, A. M., Ono, T., Pregon, A., Pierrot, D., Poulter, B., Rehder, G. ., Resplandy, L., Robertson, E., Rödenbeck, C., Séférian, R., Schwinger, J., Smith, N., Tans, P. P., Tian, H., Tilbrook, B. ., Tubiello, F. N., van der Werf, G. R., Wiltshire, A. J., and Zaehle, S.: Global Carbon Budget 2019, *Earth System Science Data*, 11, 1783–1838, <https://doi.org/10.5194/essd-11-1783-2019>, 2019.
- 850 Gadgil, S.: The Indian Monsoon and its Variability, *Annual Review of Earth and Planetary Sciences*, 31, 429–467, <https://doi.org/10.1146/annurev.earth.31.100901.141251>, 2003.
- 855 Gerbig, C., Lin, J. C., Wofsy, S. C., Daube, B. C., Andrews, A. E., Stephens, B. B., Bakwin, P. S., and Grainger, C. A.: Toward constraining regional-scale fluxes of CO<sub>2</sub> with atmospheric observations over a continent: 1. Observed spatial variability from airborne platforms, *Journal of Geophysical Research: Atmospheres*, 108, D24-4756, <https://doi.org/10.1029/2002jd003018>, 2003.
- 860 Gerbig, C., Körner, S., and Lin, J. C.: Vertical mixing in atmospheric tracer transport models: error characterization and propagation, *Atmospheric Chemistry and Physics*, 8, 591–602, <https://doi.org/10.5194/acp-8-591-2008>, 2008.

- Goswami, B. N. and Xavier, P. K.: Dynamics of “internal” interannual variability of the Indian summer monsoon in a GCM, *Journal of Geophysical Research*, 110, D24104, <https://doi.org/10.1029/2005jd006042>, 2005.
- 865
- Grell, G. A., Peckham, S. E., Schmitz, R., McKeen, S. A., Frost, G., Skamarock, W. C., and Eder, B.: Fully coupled online chemistry within the WRF model, *Atmospheric Environment*, 39, 6957-6975, <https://doi.org/10.1016/j.atmosenv.2005.04.027>, 2005.
- Hammerling, D. M., Michalak, A. M., and Kawa, S. R.: Mapping of CO<sub>2</sub> at high spatiotemporal resolution using satellite observations: Global distributions from OCO-2, *Journal of Geophysical Research*, 117, D06306, <https://doi.org/10.1029/2011JD017015>, 2012.
- 870
- Hersbach, H., Bell, B., Berrisford, P., Hirahara, S., Horányi, A., Muñoz-Sabater, J., Nicolas, Julien and Peubey, C., Radu, R., Schepers, D., Simmons, A., Soci, C., Abdalla, S., Abellan, X., Balsamo, G. o., Bechtold, P., Biavati, G., Bidlot, J., Bonavita, M., De Chiara, G., Dahlgren, P., Dee, D., Diaman takis, M., Dragani, R., Flemming, J., Forbes, R., Fuentes, M., Geer, A., Haimberger, L., Healy, S., Hogan, R. J., Hólm, E., Janisková, M., Keeley, S., Laloyaux, P., Lopez, P., Lupu, C., Radnoti, G. a., de Rosnay, P., Rozum, I., Vamborg, F., Villaume, S., and Thépaut, J.-N.: The ERA5 global reanalysis, *Quarterly Journal of the Royal Meteorological Society*, 146, 1999–2049, <https://doi.org/10.1002/qj.3803>, 2020.
- 875
- Inness, A., Ades, M., Agustí-Panareda, A., Barré, J., Benedictow, A., Blechschmidt, A.-M., Dominguez, J. J., Engelen, R., Eskes, H., Flemming, J., Huijnen, V., Jones, L., Kipling, Z., Massart, S., Parrington, M., Peuch, V.-H., Razinger, M., Remy, S., Schulz, M., and Suttie, M.: The CAMS reanalysis of atmospheric composition, *Atmospheric Chemistry and Physics*, 19, 3515–3556, <https://doi.org/10.5194/acp-19-3515-2019>, 2019.
- 880
- Jacobson, A. R., Schuldt, K. N., Miller, J. B., Oda, T., Tans, P., Arlyn Andrews, Mund, J., Ott, L., Collatz, G. J., Aalto, T., Afshar, S., Aikin, K., Aoki, S., Apadula, F., Baier, B., Bergamaschi, P., Beyersdorf, A., Biraud, S. C., Bollenbacher, A., Bowling, D., Brailsford, G., Abshire, J. B., Chen, G., Huilin Chen, Lukasz Chmura, Sites Climadat, Colomb, A., Conil, S., Cox, A., Cristofanelli, P., Cueva s, E., Curcoll, R., Sloop, C. D., Davis, K., Wekker, S. D., Delmotte, M., DiGangi, J. P., Dlugokencky, E., Ehleringer, J., Elkins, J. W., Emmenegger, L., Fischer, M. L., Forster, G., Frumau, A., Galkowski, M., Gatti, L. V., Gloor, E., Griffis, T., Hammer, S., Haszpra, L., Hatakka, J., Heliasz, M., Hensen, A., Herman ssen, O., Hintsa, E., Holst, J., Jaffe, D., Karion, A., Kawa, S. R., Keeling, R., Keronen, P., Kolari, P. a., Kominkova, K., Kort, E., Krummel, P., Kubistin, D., Labuschagne, C., Langenfelds, R., Laurent, O., La urila, T., Lauvaux, T., Law, B., Lee, J., Lehner, I., Leuenberger, M., Levin, I., Levula, J., Lin, J., Lindauer, M., Loh, Z., Lopez, M., Lujikx, I. T., Myhre, C. L., Machida, T., Mammarella, I., Man ca, G., Manning, A., Manning, A., Marek, M. V., Marklund, P., Martin, M. Y., Matsueda, H., McKain, K., Meijer, H., Meinhardt, F., Miles, N., Miller, C. E., Mölder, M., Montzka, S., Moore, F., Jose p-Anton Morgui, Morimoto, S., Munger, B., Jaroslaw Necki, Newman, S., Nichol, S., Niwa, Y., O’Doherty, S., Mikael Ottosson-Löfvenius, Paplawsky, B., Peischl, J., Peltola, O., Jean-Marc Pichon, Piper, S., Plass-Dömler, Christian and Ramonet, M., Reyes-Sanchez, E., Richardson, S., Riris, H., Ryerson, T., Saito, K., Sargent, M., Sasa kawa, M., Sawa, Y., Say, D., Scheeren, B., Schmidt, M., Schmidt, A., Schumacher, M., Shepson, P., Sh ook, M., Stanley, K., Steinbacher, M., Stephens, B., Sweeney, C., Thoning, K., Torn, M., Turnbull, J. n., Tørseth, K., Bulk, P. V. D., Dinker, D. V., Vermeulen, A.,
- 885
- 890
- 895
- 900

- Viner, B., Vitkova, G., Walker, S., Weyrauch, D., Wofsy, S., Worthy, D., Dickon Young, and Mirosław Zimnoch: CarbonTracker CT2019B, <https://doi.org/10.25925/20201008>, 2020.
- 905 Janjić, T., Bormann, N., Bocquet, M., Carton, J. A., Cohn, S. E., Dance, S. L., Losa, S. N., Nichols, N. K., Potthast, R., Waller, J. A., and Weston, P.: On the representation error in data assimilation, *Quarterly Journal of the Royal Meteorological Society*, 144, 1257–1278, <https://doi.org/10.1002/qj.3130>, 2017.
- Jung, M., Henkel, K., Herold, M., Churkina, G.: Exploiting synergies of global land cover products for carbon cycle modelling, *Remote Sensing of Environment*, 101(4), 534–553, <https://doi.org/10.1016/j.rse.2006.01.020>, 2006.
- 910 Kaiser, J. W., Heil, A., Andreae, M. O., Benedetti, A., Chubarova, N., Jones, L., Morcrette, J.-J., Razinger, M., Schultz, M. G., Suttie, M., and van der Werf, G. R.: Biomass burning emissions estimated with a global fire assimilation system based on observed fire radiative power, *Biogeosciences*, 9, 527–554, <https://doi.org/10.5194/bg-9-527-2012>, 2012.
- 915 Kretschmer, R., Gerbig, C., Karstens, U., Biavati, G., Vermeulen, A., Vogel, F., Hammer, S., and Totsche, K. U.: Impact of optimized mixing heights on simulated regional atmospheric transport of CO<sub>2</sub>, *Atmospheric Chemistry and Physics*, 14, 7149–7172, <https://doi.org/10.5194/acp-14-7149-2014>, 2014.
- Krishnamurthy, V. and Shukla, J.: Seasonal persistence and propagation of intraseasonal patterns over the Indian monsoon region, *Climate Dynamics*, 30, 353–369, <https://doi.org/10.1007/s00382-007-0300-7>, 2007.
- 920 Krishnamurthy, V. and Ajayamohan, R. S.: Composite Structure of Monsoon Low Pressure Systems and Its Relation to Indian Rainfall, *Journal of Climate*, 23, 4285–4305, <https://doi.org/10.1175/2010JCLI2953.1>, 2010.
- Kunchala, R. K., Patra, P. K., Kumar, K. N., Chandra, N., Attada, R. and Karumuri, R. K.: Spatio-temporal variability of XCO<sub>2</sub> over Indian region inferred from Orbiting Carbon Observatory (OCO-2) satellite and Chemistry Transport Model, *Atmospheric Research*, 269, 106044. <https://doi.org/10.1016/J.ATMOSRES.2022.106044>, 2022.
- 925 Lauvaux, T., Pannekoucke, O., Sarrat, C., Chevallier, F., Ciais, P., Noilhan, J., and Rayner, P. J.: Structure of the transport uncertainty in mesoscale inversions of CO<sub>2</sub> sources and sinks using ensemble model simulations, *Biogeosciences*, 6, 1089–1102, <https://doi.org/10.5194/bg-6-1089-2009>, 2009a.
- 930 Lauvaux, T., B. Gioli, C. Sarrat, P. J. Rayner, P. Ciais, F. Chevallier, J. Noilhan, F. Miglietta, Y. Brunet, E. Ceschia, H. Dolman, J. A. Elbers, C. Gerbig, R. Hutjes, N. Jarosz, D. Legain, M. Uliasz: Bridging the gap between atmospheric concentrations and local ecosystem measurements, *Geophysical Research Letters*, 36, L19809, <https://doi.org/10.1029/2009GL039574>, 2009b.
- 935 Landschützer, P., Gruber, N., and Bakker, D. C. E.: An observation-based global monthly gridded sea surface pCO<sub>2</sub> product from 1982 onward and its monthly climatology (NCEI Accession 0160558), <https://doi.org/10.7289/v5z899n6>, 2017.
- Li, D., Vogel, B., Müller, R., Bian, J., Günther, G., & Riese, M.: Tropical cyclones reduce ozone in the tropopause region over the western Pacific: An analysis of 18 years ozonesonde profiles, *Earth's Future*, 9, e2020EF001635, <https://doi.org/10.1029/2020EF001635>, 2021.
- 940 Li, W., Ciais, P., Wang, Y., Peng, S., Broquet, G., Ballantyne, A. P., Canadell, J. G., Cooper, L., Friedlingstein, P., Le Quéré, C., Myneni, R. B., Peters, G. P., Piao, S., and Pongratz, J.: Reducing uncertainties in

- decadal variability of the global carbon budget with multiple datasets, *Proceedings of the National Academy of Sciences*, 113, 13104–13108, <https://doi.org/10.1073/pnas.1603956113>, 2016.
- 945 Liang, A., Gong, W., Han, G., and Xiang, C.: Comparison of Satellite-Observed XCO<sub>2</sub> from GOSAT, OCO-2, and Ground-Based TCCON, *Remote Sensing*, 9, 1033, <https://doi.org/10.3390/rs9101033>, 2017.
- Lin, J. C., Gerbig, C., Wofsy, S. C., Andrews, A. E., Daube, B. C., Davis, K. J., and Grainger C. A.: A near-field tool for simulating the upstream influence of atmospheric observations: The Stochastic Time-Inverted Lagrangian Transport (STILT) model, *Journal of Geophysical Research: Atmospheres*, 108, 4493, <https://doi.org/10.1029/2002JD003161>, 2003.
- 950 Lin, X., Indira, N. K., Ramonet, M., Delmotte, M., Ciais, P., Bhatt, B. C., Reddy, M. V., Angechuk, D., Balakrishnan, S., Jorphail, S., Dorjai, T., Mahey, T. T., Patnaik, S., Begum, M., Brenninkmeijer, C., Durairaj, S., Kirubakaran, R., Schmidt, M., Swathi, P. S., Vinithkumar, N. V., Yver Kwok, C., and Gaur, V. K.: Long-lived atmospheric trace gases measurements in flask samples from three stations in India, *Atmospheric Chemistry and Physics*, 15, 9819–9849, <https://doi.org/10.5194/acp-15-9819-2015>, 2015.
- 955 Liu, Y., Yue, T., Zhang, L., Zhao, N., Zhao, M., and Liu, Y.: Simulation and analysis of XCO<sub>2</sub> in North China based on high accuracy surface modeling, *Environmental Science and Pollution Research*, 25, 27378–27392, <https://doi.org/10.1007/s11356-018-2683-x>, 2018.
- 960 Mahadevan, P., Wofsy, S. C., Matross, D. M., Xiao, X., Dunn, A. L., Lin, J. C., Gerbig, C., Munger, J.W., Chow, V. Y., and Gottlieb, E.W.: A satellite-based biosphere parameterization for net ecosystem CO<sub>2</sub> exchange: Vegetation Photosynthesis and Respiration Model (VPRM), *Global Biogeochemical Cycles*, 22, GB2005, <https://doi.org/10.1029/2006gb002735>, 2008.
- 965 Massart, S., Agustí-Panareda, A., Heymann, J., Buchwitz, M., Chevallier, F., Reuter, M., Hilker, M., Burrows, J. P., Deutscher, N. M., Feist, D. G., Hase, F., Sussmann, R., Desmet, F., Dubey, M. K., Griffith, D. W. T., Kivi, R., Petri, C., Schneider, M., and Velasco, V. A.: Ability of the 4-D-Var analysis of the GOSAT BESD XCO<sub>2</sub> retrievals to characterize atmospheric CO<sub>2</sub> at large and synoptic scales, *Atmospheric Chemistry and Physics*, 16, 1653–1671, <https://doi.org/10.5194/acp-16-1653-2016>, 2016.
- 970 McKain, K., Wofsy, S. C., Nehrkorn, T., Eluszkiewicz, J., Ehleringer, J. R., and Stephens, B. B.: Assessment of ground-based atmospheric observations for verification of greenhouse gas emissions from an urban region, *Proceedings of the National Academy of Sciences*, 109, 8423–8428, <https://doi.org/10.1073/pnas.1116645109>, 2012.
- 975 Miller, C. E., Crisp, D., DeCola, P. L., Olsen, S. C., Randerson, J. T., Michalak, A. M., Alkhaled, A., Rayner, P., Jacob, D. J., Suntharalingam, P., Jones, D. B. A., Denning, A. S., Nicholls, M. E., Doney, S. C., Pawson, S., Boesch, H., Connor, B. J., Fung, I. Y., O'Brien, D., Salawitch, R. J., Sander, S. P., Sen, B., Tans, P., Toon, G. C., Wennberg, P. O., Wofsy, S. C., Yung, Y. L., Law, R. M.: Precision requirements for space-based XCO<sub>2</sub> data, *Journal of Geophysical Research*, 112, D10314, <https://doi.org/10.1029/2006JD007659>, 2007.
- 980 NOAA/ESRL: Dipole Mode Index, available at: [https://www.esrl.noaa.gov/psd/gcos\\_wgsp/Timeseries/DMI/](https://www.esrl.noaa.gov/psd/gcos_wgsp/Timeseries/DMI/), last access: 11 February 2022a.
- NOAA/ESRL: Multivariate ENSO Index, available at: <https://www.esrl.noaa.gov/psd/enso/mei/>, last access: 11 February 2022b.

- Nomura, S., Naja, M., Ahmed, M. K., Mukai, H., Terao, Y., Machida, T., Sasakawa, M., and Patra, P. K.: Measurement report: Regional characteristics of seasonal and long-term variations in greenhouse gases at Nainital, India, and Comilla, Bangladesh, *Atmos. Chem. Phys.*, 21, 16427–16452, <https://doi.org/10.5194/acp-21-16427-2021>, 2021.
- 985
- O’Dell, Connor, B., Bösch, H., O’Brien, D., Frankenberg, C., Castano, R., Christi, M., Eldering, D., Fisher, B., Gunson, M., McDuffie, J., Miller, C. E., Natraj, V., Oyafuso, F., Polonsky, I., Smyth, M., Taylor, T., Toon, G. C., Wennberg, P. O., and Wunch, D.: The ACOS CO<sub>2</sub> retrieval algorithm – Part 1: Description and validation against synthetic observations, *Atmospheric Measurement Techniques*, 5, 99–121, <https://doi.org/10.5194/amt-5-99-2012>, 2012.
- 990
- Parazoo, N. C., Denning, A. S., Berry, J. A., Wolf, A., 625 Randall, D. A., Kawa, S. R., Pauluis, O., and Doney, S. C.: Moist synoptic transport of CO<sub>2</sub> along the mid-latitude storm track, *Geophysical Research Letters*, 38, L09804, <https://doi.org/10.1029/2011gl047238>, 2011.
- 995
- Park, M., Randel, W. J., Gettelman, A., Massie, S. T., and Jiang, J. H.: Transport above the Asian summer monsoon anticyclone inferred from Aura Microwave Limb Sounder tracers, *Journal of Geophysical Research*, 112, D16309, <https://doi.org/10.1029/2006JD008294>, 2007.
- Park, C., Gerbig, C., Newman, S., Ahmadov, R., Feng, S., Gurney, K. R., Carmichael, G. R., Park, S.-Y., Lee, H.-W., Goulden, M., Stutz, J., Peischl, J., and Ryerson, T.: CO<sub>2</sub> Transport Variability, and Budget over the Southern California Air Basin Using the High-Resolution WRF-VPRM Model during the CalNex 2010 Campaign, *Journal of Applied Meteorology and Climatology*, 57, 1337–1352, <https://doi.org/10.1175/jamc-d-17-0358.1>, 2018.
- 1000
- Park, S., Klemp, J. B., & Kim, J.: Hybrid Mass Coordinate in WRF-ARW and Its Impact on Upper-Level Turbulence Forecasting, *Monthly Weather Review*, 147(3), 971-985, <https://doi.org/10.1175/MWR-D-18-0334.1>, 2019.
- 1005
- Patra, P. K., Ishizawa, M., Maksyutov, S., Nakazawa, T., and Inoue, G.: Role of biomass burning and climate anomalies for land-atmosphere carbon fluxes based on inverse modeling of atmospheric CO<sub>2</sub>, *Global Biogeochemical Cycles*, 19, GB3005, <https://doi.org/10.1029/2004gb002258>, 2005.
- Patra, P. K., Niwa, Y., Schuck, T. J., Brenninkmeijer, C. A. M., Machida, T., Matsueda, H., and Sawa, Y.: Carbon balance of South Asia constrained by passenger aircraft CO<sub>2</sub> measurements, *Atmospheric Chemistry and Physics*, 11, 4163–4175, <https://doi.org/10.5194/acp-11-4163-2011>, 2011.
- 1010
- Peters, W., Jacobson, A. R., Sweeney, C., Andrews, A. E., Conway, T. J., Masarie, K., Miller, J. B., Bruhwiler, L. M. P., Petron, G., Hirsch, A. I., Worthy, D. E. J., van der Werf, G. R., Randerson, J. T., Wennberg, P. O., Krol, M. C., and Tans, P. P.: An atmospheric perspective on North American carbon dioxide exchange: CarbonTracker, *Proceedings of the National Academy of Sciences*, 104, 18925–18930, <https://doi.org/10.1073/pnas.0708986104>, 2007.
- 1015
- Philip, S., Johnson, M. S., Baker, D. F., Basu, S., Tiwari, Y. K., Indira, N. K., Ramonet, M. and Poulter, B.: OCO-2 satellite-imposed constraints on terrestrial biospheric CO<sub>2</sub> fluxes over South Asia. *Journal of Geophysical Research: Atmospheres*, 127, e2021JD035035. <https://doi.org/10.1029/2021JD035035>.
- 1020

- Pillai, D., Gerbig, C., Marshall, J., Ahmadov, R., Kretschmer, R., Koch, T., and Karstens, U.: High resolution modeling of CO<sub>2</sub> over Europe: implications for representation errors of satellite retrievals, *Atmospheric Chemistry and Physics*, 10, 83–94, <https://doi.org/10.5194/acp-10-83-2010>, 2010.
- 1025 Pillai, D., Gerbig, C., Ahmadov, R., Rödenbeck, C., Kretschmer, R., Koch, T., Thompson, R., Neininger, B., and Lavrié, J. V.: High-resolution simulations of atmospheric CO<sub>2</sub> over complex terrain – representing the Ochsenkopf mountain tall tower, *Atmospheric Chemistry and Physics*, 11, 7445–7464, <https://doi.org/10.5194/acp-11-7445-2011>, 2011.
- 1030 Pillai, D., Gerbig, C., Kretschmer, R., Beck, V., Karstens, U., Neininger, B., and Heimann, M.: Comparing Lagrangian and Eulerian models for CO<sub>2</sub> transport – a step towards Bayesian inverse modeling using WRF/STILT-VPRM, *Atmospheric Chemistry and Physics*, 12, 8979–8991, <https://doi.org/10.5194/acp-12-8979-2012>, 2012.
- 1035 Pillai, D., Buchwitz, M., Gerbig, C., Koch, T., Reuter, M., Bovensmann, H., Marshall, J., and Burrows, J. P.: Tracking city CO<sub>2</sub> emissions from space using a high-resolution inverse modelling approach: a case study for Berlin, Germany, *Atmospheric Chemistry and Physics*, 16, 9591–9610, <https://doi.org/10.5194/acp-16-9591-2016>, 2016.
- Ravi Kumar, K., Valsala, V., Tiwari, Y. K., Revadekar, J. V., Pillai, P., Chakraborty, S., and Murtugudde, R.: Intra-seasonal variability of atmospheric CO<sub>2</sub> concentrations over India during summer monsoons, *Atmospheric Environment*, 142, 229–237, <https://doi.org/10.1016/j.atmosenv.2016.07.023>, 2016.
- 1040 Rödenbeck, C., Houweling, S., Gloor, M., and Heimann, M.: CO<sub>2</sub> flux history 1982–2001 inferred from atmospheric data using a global inversion of atmospheric transport, *Atmospheric Chemistry and Physics*, 3, 1919–1964, <https://doi.org/10.5194/acp-3-1919-2003>, 2003.
- Rödenbeck, C., Zaehle, S., Keeling, R., and Heimann, M.: How does the terrestrial carbon exchange respond to inter-annual climatic variations? A quantification based on atmospheric CO<sub>2</sub> data, *Biogeosciences*, 15, 2481–2498, <https://doi.org/10.5194/bg-15-2481-2018>, 2018a.
- 1045 Rödenbeck, C., Zaehle, S., Keeling, R., and Heimann, M.: History of El Niño impacts on the global carbon cycle 1957–2017: a quantification from atmospheric CO<sub>2</sub> data, *Phil. Trans. R. Soc. B*, 373, 20170303, <https://doi.org/10.1098/rstb.2017.0303>, 2018b.
- 1050 Sarrat, C., Noilhan, J., Dolman, A. J., Gerbig, C., Ahmadov, R., Tolk, L. F., Meesters, A. G. C. A., Hutjes, R. W. A. and Ter Maat, H. W., Pérez-Landa, G., and Donier, S.: Atmospheric CO<sub>2</sub> modeling at the regional scale: an intercomparison of 5 meso-scale atmospheric models, *Biogeosciences*, 4, 1115–1126, <https://doi.org/10.5194/bg-4-1115-2007>, 2007.
- 1055 Schimel, D. S., House, J. I., Hibbard, K. A., Bousquet, P., 665 Ciais, P., Peylin, P., Braswell, B. H., Apps, M. J., Baker, D., Bondeau, A., Canadell, J., Churkina, G., Cramer, W., Denning, A. S., Field, C. B., Friedlingstein, P., Goodale, C., Heimann, M., Houghton, R. A., Melillo, J. M., Moore, B., Murdiyarso, D., Noble, I., Pacala, S. W., Prentice, I. C., Raupach, M. R., Rayner, P. J., Scholes, R. J., Steffen, W. L., and Wirth, C.: Recent patterns and mechanisms of carbon exchange by terrestrial ecosystems, *Nature*, 414, 169–172, <https://doi.org/10.1038/35102500>, 2001.
- 1060 Schimel, D., Stephens, B. B., and Fisher, J. B.: Effect of increasing CO<sub>2</sub> on the terrestrial carbon cycle, *Proceedings of the National Academy of Sciences*, 112, 436–441, <https://doi.org/10.1073/pnas.1407302112>, 2014.

- Skamarock, W. C., Klemp, J. B., Dudhia, J., Gill, D. O., Duda, D. M. B. M. G., Huang, X.-Y., Wang, W., and Powers, J. G.: A description of the advanced research WRF version 3, NCAR Tech. Note, NCAR/TN-468+STR, Tech. rep., National Center for Atmosphere Research, Boulder, Colorado, USA, <https://doi.org/doi:10.5065/D68S4MVH>, 2008.
- 1065 Skamarock, W. C., Klemp, J. B., Dudhia, J., Gill, D. O., Liu, Z., Berner, J., Wang, W., Powers, J. G., Duda, M. G., Barker D. M., Huang, X. -yu.: A Description of the Advanced Research WRF Model Version 4.3., <https://doi:10.5065/1dfh-6p97>, 2021.
- Steinbach, J., Gerbig, C., Rödenbeck, C., Karstens, U., Minejima, C., and Mukai, H.: The CO<sub>2</sub> release and Oxygen uptake from Fossil Fuel Emission Estimate (COFFEE) dataset: effects from varying oxidative ratios, *Atmospheric Chemistry and Physics*, 11, 6855–6870, <https://doi.org/10.5194/acp-11-6855-2011>, 2011.
- 1070 Takahashi, T., Sutherland, S. C., Wanninkhof, R., Sweeney, C., Feely, R. A., Chipman, D. W., and Gernot Friederich, B. H., Chavez, F., Sabine, C., Watson, A., Bakker, D. C., Schuster, U., Metzl, N., Yoshikawa-Inoue, H., Ishii, M., Midorikawa, T., Nojiri, Y., Körtzinger, A., Steinhoff, T., and Jon Olafsson, M. H., Arnarson, T. S., Tilbrook, B., Johannessen, T., Olsen, A., Bellerby, R., Wong, C., Ile, B. D., Bates, N., and de Baar, H. J.: Climatological mean and decadal change in surface ocean pCO<sub>2</sub>, and net sea–air CO<sub>2</sub> flux over the global oceans, *Deep Sea Research Part II: Topical Studies in Oceanography*, 56, 554 – 577, <https://doi.org/10.1016/j.dsr2.2008.12.009>, 2009.
- 1075 Tiwari Y. K., Patra P. K., Chevallier F., Francey R. J., Krummel P. B., Allison C. E., Revadekar J. V., Chakraborty S., Langenfelds R. L., Bhattacharya S. K., Borole D. V., Kumar K. R. and Steele L. P.: CO<sub>2</sub> observations at Cape Rama, India for the period of 1993–2002: implications for constraining Indian emissions. *Current Science, Indian Academy of Sciences*, 101, 1562–1568, 2011
- 1080 Tiwari, Y. K., Revadekar, J. V., and Kumar, K. R.: Variations in atmospheric Carbon Dioxide and its association with rainfall and vegetation over India. *Atmospheric Environment*, 68, 45–51. <https://doi.org/10.1016/j.atmosenv.2012.11.040>, 2013.
- 1085 Thilakan, V. and Pillai, D.: Representation error in global model CO<sub>2</sub> simulations over India [Data set], Zenodo, <https://doi.org/10.5281/zenodo.6616466>, 2022.
- Tolk, L. F., Meesters, A. G. C. A., Dolman, A. J., and Peters, W.: Modelling representation errors of atmospheric CO<sub>2</sub> mixing ratios at a regional scale, *Atmospheric Chemistry and Physics*, 8, 6587–6596, <https://doi.org/10.5194/acp-8-6587-2008>, 2008.
- 1090 Uebel, M., Herbst, M. and Bott, A.: Mesoscale simulations of atmospheric CO<sub>2</sub> variations using a high-resolution model system with process-based CO<sub>2</sub> fluxes. *Q.J.R. Meteorol. Soc.*, 143: 1860-1876. <https://doi.org/10.1002/qj.3047>, 2017.
- 1095 Valsala, V. and Maksyutov, S.: Interannual variability of the air–sea CO<sub>2</sub> flux in the north Indian Ocean, *Ocean Dynamics*, 63, 165–178, <https://doi.org/10.1007/s10236-012-0588-7>, 2013.
- van der Molen, M. K. and Dolman, A. J.: Regional carbon fluxes and the effect of topography on the variability of atmospheric CO<sub>2</sub>, *Journal of Geophysical Research*, 112, D01104, <https://doi.org/10.1029/2006jd007649>, 2007.

- 1100 Vogel, B., Müller, R., Günther, G., Spang, R., Hanumanthu, S., Li, D., Riese, M., and Stiller, G. P.: Lagrangian simulations of the transport of young air masses to the top of the Asian monsoon anticyclone and into the tropical pipe, *Atmos. Chem. Phys.*, 19, 6007–6034, <https://doi.org/10.5194/acp-19-6007-2019>, 2019.
- 1105 Willetts, P.D., Marsham, J.H., Birch, C.E., Parker, D.J., Webster, S. and Petch, J.: Moist convection and its upscale effects in simulations of the Indian monsoon with explicit and parametrized convection. *Q.J.R. Meteorol. Soc.*, 143, 1073-1085, <https://doi.org/10.1002/qj.2991>, 2017.
- 1110 Wunch, D., Wennberg, P. O., Osterman, G., Fisher, B., Naylor, B., Roehl, C. M., O'Dell, C., Mandrake, L., Viatte, C., Kiel, M., Griffith, D. W. T., Deutscher, N. M., Velazco, V. A., Notholt, J., Warneke, T., Petri, C., De Maziere, M., Sha, M. K., Sussmann, R., Rettinger, M., Pollard, D., Robinson, J., Morino, I., Uchino, O., Hase, F., Blumenstock, T., Feist, D. G., Arnold, S. G., Strong, K., Mendonca, J., Kivi, R., Heikkinen, P., Iraci, L., Podolske, J., Hillyard, P. W., Kawakami, S., Dubey, M. K., Parker, H. A., Sepulveda, E., Garcia, O. E., Te, Y., Jeseck, P., Gunson, M. R., Crisp, D., and Eldering, A.: Comparisons of the Orbiting Carbon Observatory-2 (OCO-2) XCO<sub>2</sub> measurements with TCCON, *Atmospheric Measurement Techniques*, 10, 2209–2238, <https://doi.org/10.5194/amt-10-2209-2017>, 2017.
- 1115 Zellweger, C., Emmenegger, L., Firdaus, M., Hatakka, J., Heimann, M., Kozlova, E., Spain, T. G., Steinbacher, M., van der Schoot, M. V., and Buchmann, B.: Assessment of recent advances in measurement techniques for atmospheric carbon dioxide and methane observations, *Atmos. Meas. Tech.*, 9, 4737–4757, <https://doi.org/10.5194/amt-9-4737-2016>, 2016.
- 1120

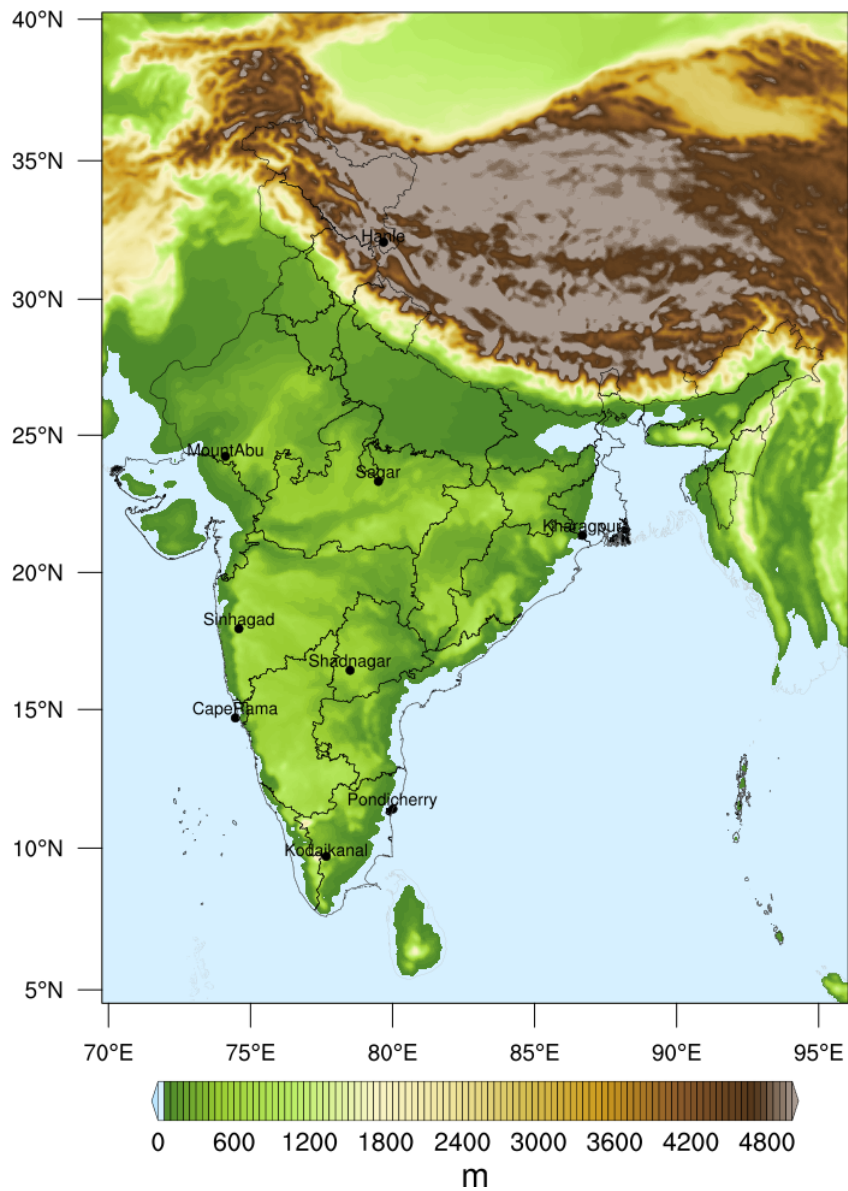
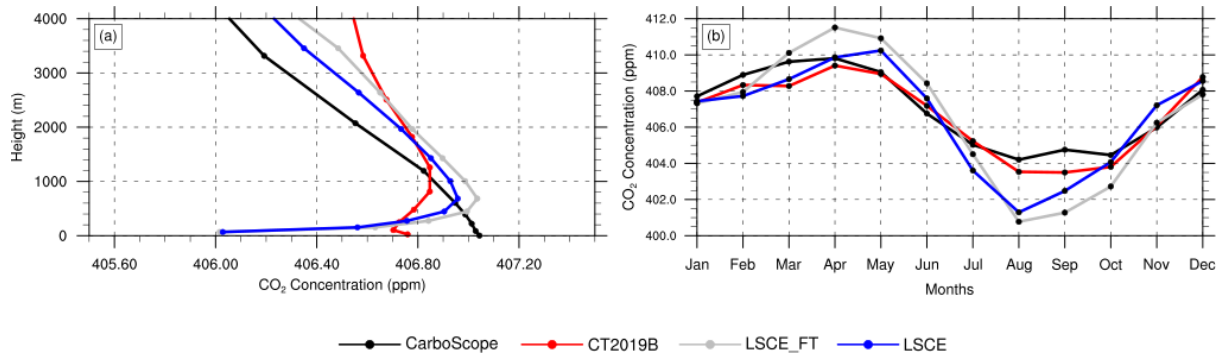


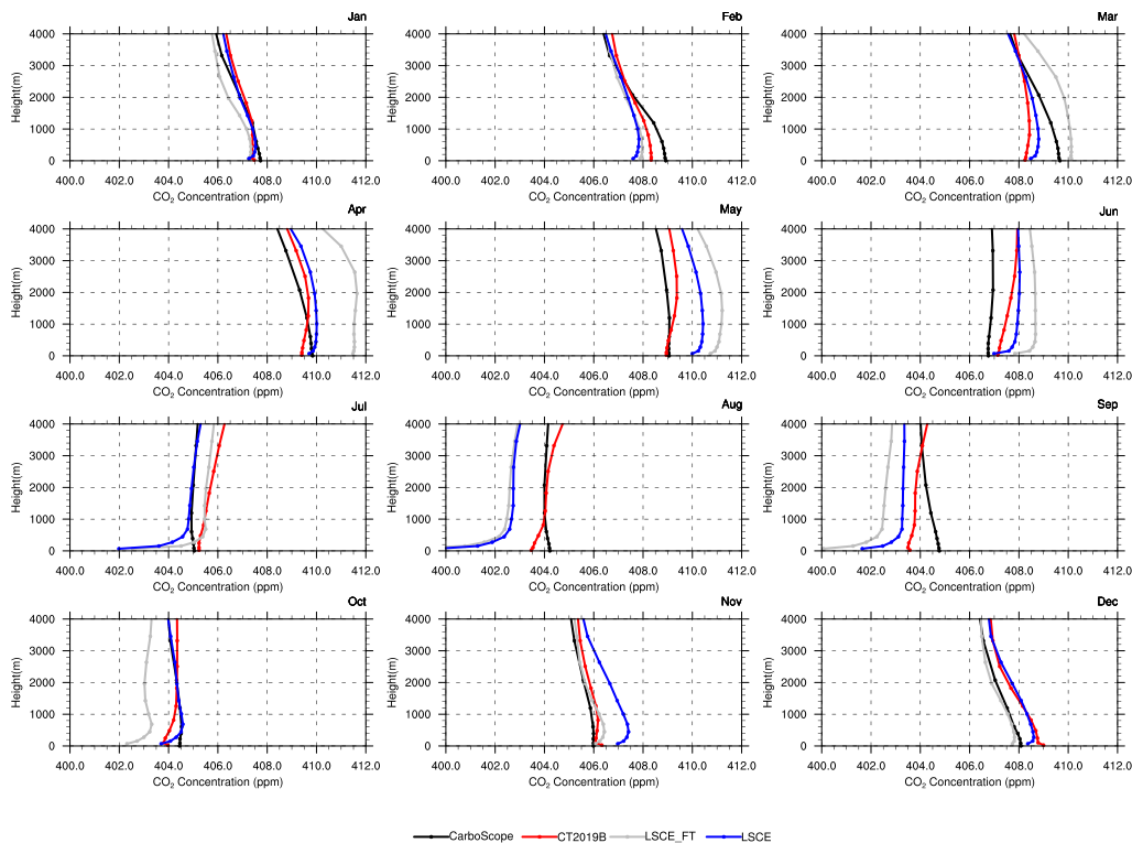
**Figure 1: The WRF-GHG model domain used in this study, showing topography. The CO<sub>2</sub> monitoring sites over India used for the OSSE experiments are marked. Not all these observation stations are currently fully operational. The colour scale is restricted to 5000 m for the better visualization of terrain details over the Indian subcontinent.**

1125



1130

**Figure 2: Comparison of global models over the model domain during daytime (11:30 to 16:30 local time) in 2017. a) Annually averaged vertical profiles of CO<sub>2</sub> concentration in the lower troposphere b) Time series of monthly averaged CO<sub>2</sub> concentration at surface (~100 m above surface).**



1135

**Figure 3: Comparison of average monthly vertical profiles of CO<sub>2</sub> concentration from global atmospheric transport models over the model domain during daytime (11:30 to 16:30 local time) in 2017. Panels show data for respective months as indicated on the top of each panel.**

1140

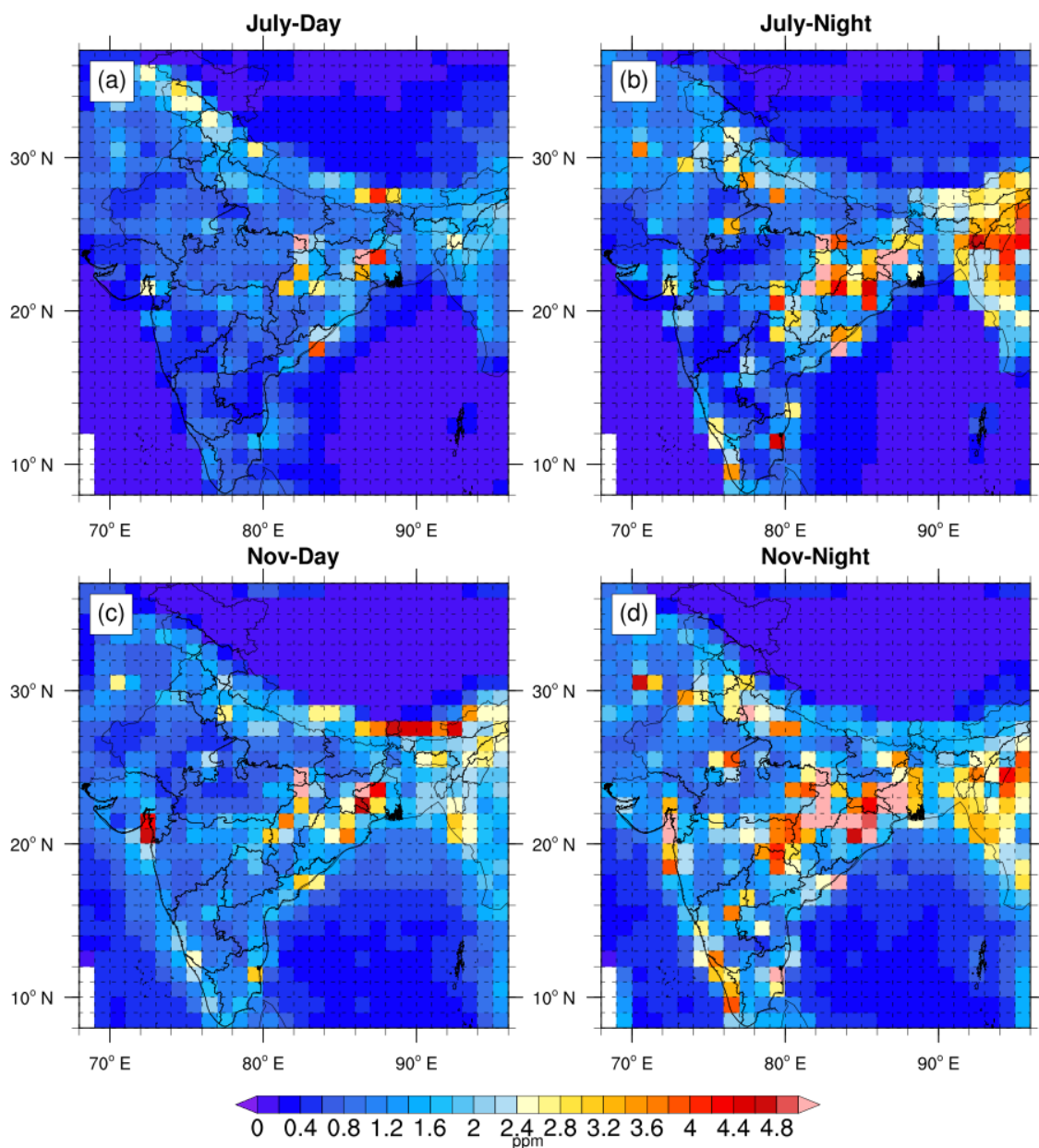
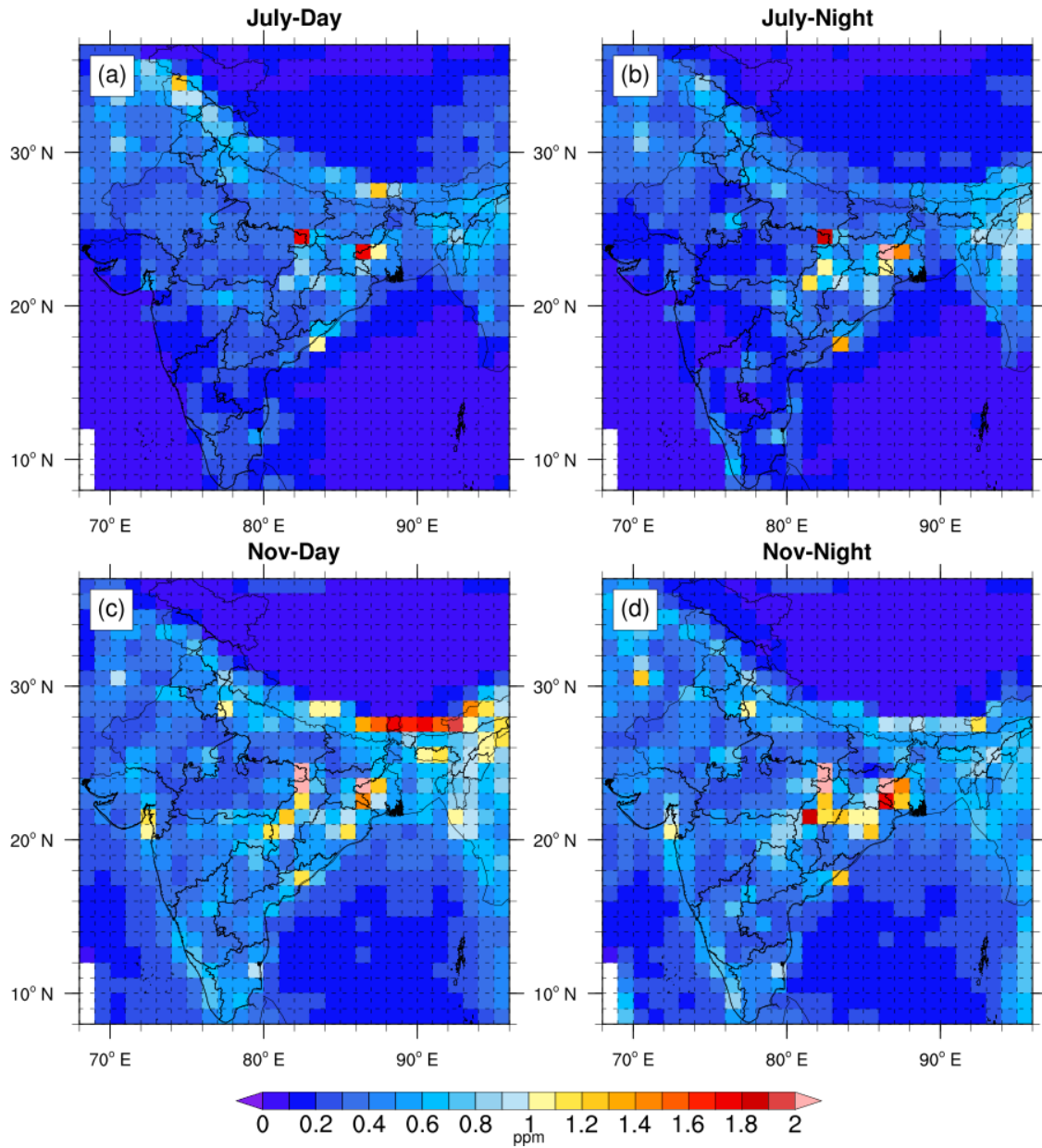
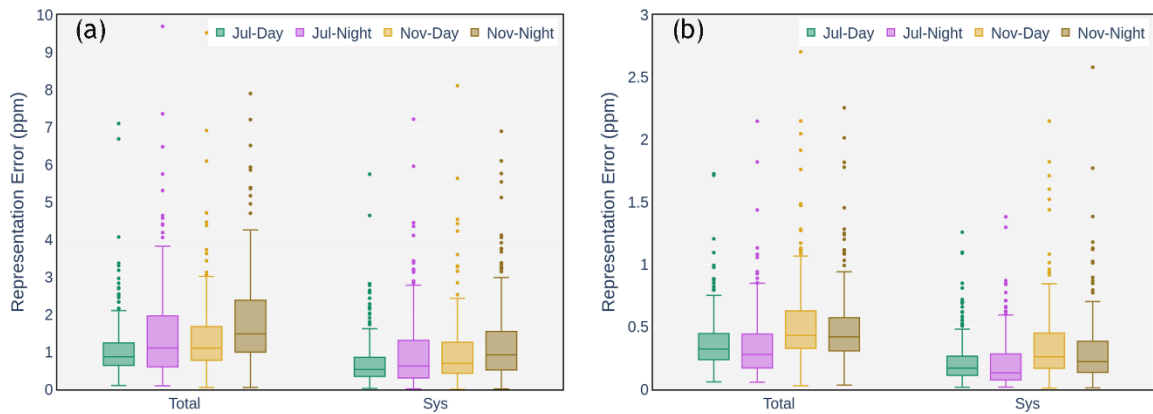


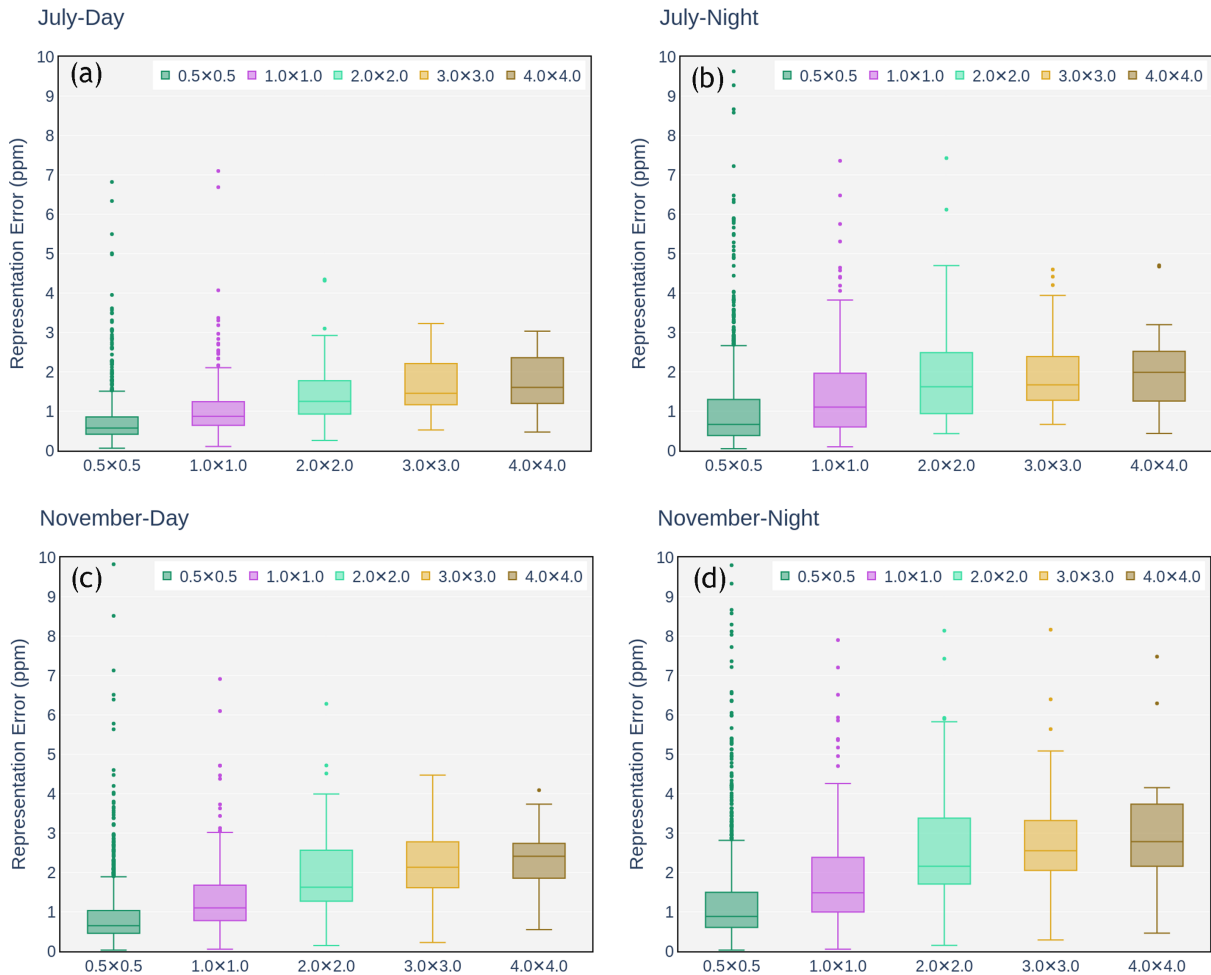
Figure 4: Monthly averaged values of representation error estimated for surface CO<sub>2</sub> concentration (second model level, mean height is ~200 m from sea level) over the region 8° N to 37° N and 68° E to 96° E during 2017. a) July daytime (11:30 to 16:30 local time) b) July nighttime (23:30 to 4:30 local time). c) November daytime. d) November nighttime.



1160 **Figure 5: Monthly averaged values of representation error estimated for column averaged CO<sub>2</sub> concentration over the region 8° N to 37° N and 68° E to 96° E during 2017. a) July daytime (11:30 to 16:30 local time) b) July nighttime (23:30 to 4:30 local time). c) November daytime. d) November nighttime.**

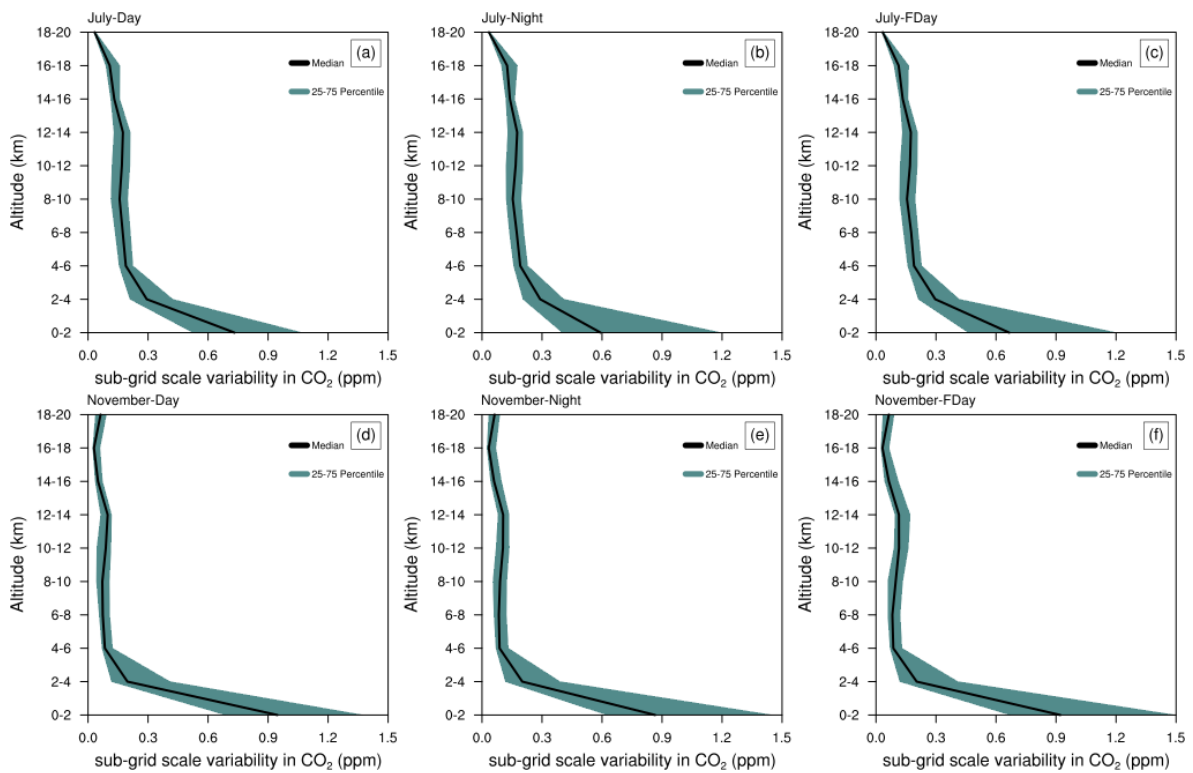


1170 **Figure 6: Variability of derived representation error over India in July and November 2017 (both during daytime and nighttime). Boxes indicate the central 50%, the bar across the box is the median value, and the whiskers indicate the values between 5 and 95 percentiles. Individual data points shown are the outliers. a) Representation error estimated for the surface CO<sub>2</sub>. b) Representation error estimated for the column averaged CO<sub>2</sub>.**



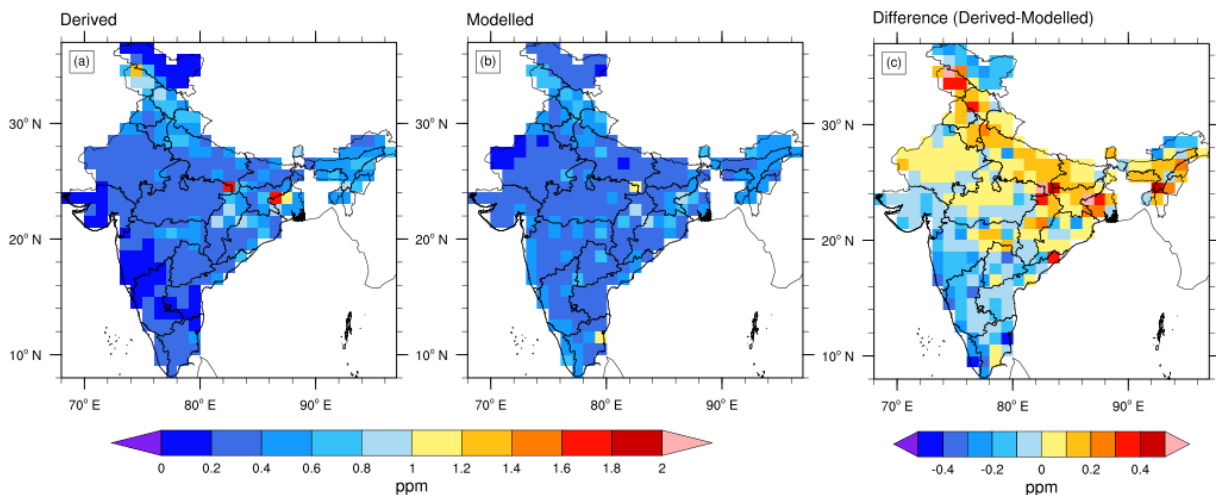
1175 **Figure 7: Variability of derived surface representation error over India for different horizontal resolutions. Boxes indicate the central 50%, the bar across the box is median value, and the whiskers indicate the value between 5 and 95 percentiles. Individual data points shown are the outliers. a) Representation error estimated for July daytime. b) July nighttime. c) November daytime. d) November nighttime.**

1180



1185

**Figure 8: Variability of representation error over India with altitude for July and November 2017. a) July daytime, b) July nighttime, c) July full time, d) November daytime, e) November nighttime, and f) November full time. Median values are plotted with black curves and the shaded region indicates 25 to 75 percentiles of data.**



1190

**Figure 9: Monthly averaged values of representation error estimated for column averaged CO<sub>2</sub> concentration during July daytime (11:30 to 16:30 local time) in 2017. a) Representation error derived from WRF-GHG simulations as explained in Sect. 2.3. b) Representation error calculated from the multivariate linear model as described in Sect. 3.5. c) Difference between (a) and (b).**

Domain						
Configuration	Single domain with horizontal resolution of 10 km; 39 vertical levels; 307 × 407 grid points					
Vertical coordinates	Terrain-following hydrostatic pressure vertical coordinates					
Basic equations	non-hydrostatic; compressible					
Grid type	Arakawa-C grid					
Time integration	3rd order Runge-Kutta split-explicit					
Spatial integration	3rd and 5th order differencing for vertical and horizontal advection respectively; both for					
Time step	momentum and scalars 60 s					
Physics schemes						
Radiation	Rapid Radiative Transfer Model (RRTM) for Longwave & Dudhia for shortwave					
Microphysics	WSM 3-classic simple ice scheme					
PBL	YSU					
Surface layer	Monin-Obukhov					
Land-surface	NOAH LSM					
Cumulus	Grell-Freitas ensemble scheme					
Emission fields						
Flux type	Product	Version	Spatial resolution	Temporal resolution	Source/website	Reference
Anthropogenic	EDGAR	v4.3	10km	Annual	<a href="https://edgar.jrc.ec.europa.eu/">https://edgar.jrc.ec.europa.eu/</a>	Crippa et al., (2018)
Biomass burning	GFAS	v1.2	10km	Daily	<a href="http://apps.ecmwf.int/datasets/data/cams-gfas/">http://apps.ecmwf.int/datasets/data/cams-gfas/</a>	Kaiser et al., (2012)
Biospheric	VPRM		Adapted to model	Adapted to model		Mahadevan et al., (2008)
Initial and Lateral Boundary conditions						
Field	Product	Version	Spatial resolution	Temporal resolution	Source/website	Reference
Meteorology	ERA5	n/a	25km	1hour	<a href="https://cds.climate.copernicus.eu/cdsapp#!/home">https://cds.climate.copernicus.eu/cdsapp#!/home</a>	Hersbach et al., (2020)
Tracer	ECMWF /CAMS	gqiq	50km	6hour	<a href="http://atmosphere.copernicus.eu">http://atmosphere.copernicus.eu</a>	Agustí-Panareda et al., (2019)

1200 **Table 2: Specifications of different global model products used in this study**

Data availability								
Product	Version	Spatial resolution	Vertical levels	Temporal resolution	Source/website	Reference		
Carbon Tracker	CT2019B	3 × 2	25	3 hours	<a href="http://carbontracker.noaa.gov">http://carbontracker.noaa.gov</a>	Jacobson et al., (2020)		
CarboScope	s10oc_v2020	5 × 3.8	19	6 hours	<a href="http://www.bgc-jena.mpg.de/CarboScope/">http://www.bgc-jena.mpg.de/CarboScope/</a>	Rödenbeck et al., (2003)		
LSCE	v18r3	3.7 × 1.8	39	3 hours	<a href="http://atmosphere.copernicus.eu">http://atmosphere.copernicus.eu</a>	Chevallier et al., (2019)		
LSCE	FT18r1	3.7 × 1.8	39	3 hours	<a href="http://atmosphere.copernicus.eu">http://atmosphere.copernicus.eu</a>	Chevallier et al., (2019)		
Data used in the inverse model simulations								
Product	Version	Forward Model	Meteorology	Observation data	Anthropogenic emission fields	Biospheric emission	Fire emission	Oceanic emission
Carbon Tracker	CT2019B	TM5	ECMWF	Ground based	Miller and ODIAC	CASA	GFED and GFED CMS	OIF and Takahashi et al., (2009)
CarboScope	s10oc_v2020	TM3	NCEP	Ground based	EDGAR	LPJ Biosphere Model	CDIAC	SOCAT
LSCE/PyVar	v18r3	LMDz6A	ECMWF	Ground based	EDGAR, CDIAC and GCP	ORCHID EE 4.6.9.5	GFED and GFAS	Denvil-Sommer et al., (2019) with updates described in Friedlingstein et al., (2019)
LSCE/PyVar	FT18r1	LMDz6A	ECMWF	Satellite (OCO-2 NASA)	EDGAR, CDIAC and GCP	ORCHID EE 1.9.5.2	GFED and GFAS	Landschutzer et al., (2018)

1205

**Table 3: Flux uncertainty over India calculated from the OSSE experiments using pseudo-observation network of surface observations. The time filter indicates the time of the data sampled for estimation of the scaling factors. Full day – 24 hours in each day; Daytime – 11:30 to 16:30 local time; Nighttime – 23:30 to 4:30 local time. \* The fraction of uncertainty to the total NEE.**

1210

Month	Time filter	True flux, aggregated over India. $\sum_{k=1}^K \Phi_{true}$ (MtCO <sub>2</sub> per month)	Flux uncertainty $S_{rep}$ (MtCO <sub>2</sub> per month) In brackets: fraction of uncertainty* (%)
July	Daytime observations	-373.31	38.59 (10.33)
July	Nighttime observations		30.14 (8.07)
July	Full day observations		23.20 (6.21)
November	Daytime observations	-417.12	18.42 (4.4)
November	Nighttime observations		13.34 (3.1)
November	Full Day observations		13.48 (3.2)

1215